



HHS Public Access

Author manuscript

Cell Rep. Author manuscript; available in PMC 2020 March 02.

Published in final edited form as:

Cell Rep. 2020 February 18; 30(7): 2360–2373.e5. doi:10.1016/j.celrep.2020.01.055.

Distinct Dorsal and Ventral Hippocampal CA3 Outputs Govern Contextual Fear Discrimination

Antoine Besnard^{1,2,3}, Samara M. Miller^{1,2,3}, Amar Sahay^{1,2,3,4,5,*}

¹Center for Regenerative Medicine, Massachusetts General Hospital, Boston, MA 02114, USA

²Harvard Stem Cell Institute, Cambridge, MA 02138, USA

³Department of Psychiatry, Massachusetts General Hospital, Harvard Medical School, Boston, MA 02114, USA

⁴BROAD Institute of Harvard and MIT, Cambridge, MA 02142, USA

⁵Lead Contact

SUMMARY

Considerable work emphasizes a role for hippocampal circuits in governing contextual fear discrimination. However, the intra- and extrahippocampal pathways that route contextual information to cortical and subcortical circuits to guide adaptive behavioral responses are poorly understood. Using terminal-specific optogenetic silencing in a contextual fear discrimination learning paradigm, we identify opposing roles for dorsal CA3-CA1 (dCA3-dCA1) projections and dorsal CA3-dorsolateral septum (dCA3-DLS) projections in calibrating fear responses to certain and ambiguous contextual threats, respectively. Ventral CA3-DLS (vCA3-DLS) projections suppress fear responses in both certain and ambiguous contexts, whereas ventral CA3-CA1 (vCA3-vCA1) projections promote fear responses in both these contexts. Lastly, using retrograde monosynaptic tracing, *ex vivo* electrophysiological recordings, and optogenetics, we identify a sparse population of DLS parvalbumin (PV) neurons as putative relays of dCA3-DLS projections to diverse subcortical circuits. Taken together, these studies illuminate how distinct dCA3 and vCA3 outputs calibrate contextual fear discrimination.

Graphical Abstract

This is an open access article under the CC BY-NC-ND license (<http://creativecommons.org/licenses/by-nc-nd/4.0/>).

* Correspondence: asahay@mgh.harvard.edu.

AUTHOR CONTRIBUTIONS

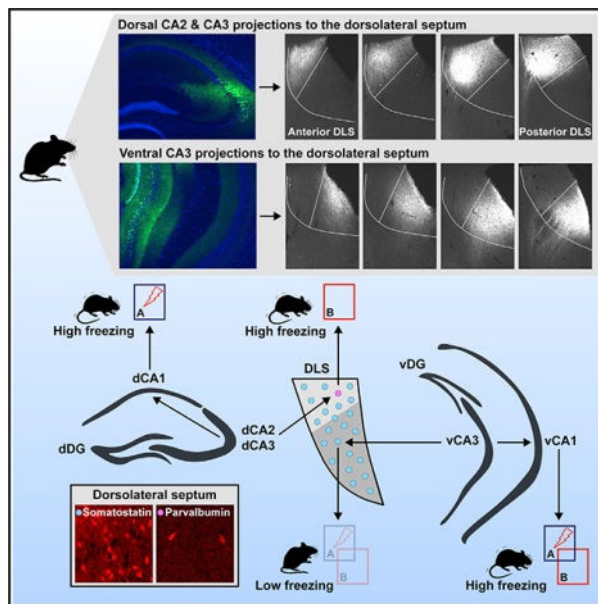
A.B. and S.M.M. performed experiments. A.S. and A.B. co-developed the concept, analyzed data, and wrote the manuscript. A.S. conceived the project and supervised all aspects of the project.

SUPPLEMENTAL INFORMATION

Supplemental Information can be found online at <https://doi.org/10.1016/j.celrep.2020.01.055>.

DECLARATION OF INTERESTS

The authors declare no competing financial and non-financial interests.



In Brief

Besnard et al. show that dorsal and ventral hippocampal CA3 projections to CA1 and dorsolateral septum (DLS) play distinct roles in calibration of contextual fear discrimination. DLS parvalbumin inhibitory neurons receive monosynaptic dorsal CA3 inputs and modulate fear responses in a context-specific manner.

INTRODUCTION

Adaptive navigation of our external world requires an assessment of contextual information pertaining to threat. When danger is clear and certain, defensive behavioral responses are deployed to permit survival. On the other hand, when threat is ambiguous, efficient discrimination is required for adaptive generalization of fear responses so that the organism is poised for pausing, flight, or fight. The hippocampus (HC) is thought to play a critical role in this process by encoding contextual information and relaying it to brain regions that mediate fear and stress responses (Kim and Fanselow, 1992; Maren et al., 2013). Specifically, the dorsal (septal) HC (dHC) is thought to mediate encoding and discrimination of contextual information, exploration, and navigation (Bannerman et al., 2014; Fanselow and Dong, 2010; Frankland et al., 1998; Kheirbek et al., 2013; McHugh et al., 2007; Strange et al., 2014), and the ventral HC (vHC; temporal) processes information underlying goal-directed behaviors and innate anxiety (Ciocchi et al., 2015; Fanselow and Dong, 2010; Jimenez et al., 2018; Kheirbek et al., 2013; Strange et al., 2014). Together, this division of labor along the septotemporal axis of the HC in rodents is thought to calibrate adaptive fear responses or defensive behavior, such as immobility (high levels of freezing behavior) when threat is certain (e.g., context associated with a mild footshock) and increased mobility (low levels of freezing behavior) to ambiguous, non-threatening stimuli in the environment (e.g., a similar neutral context not associated with a footshock). However, the dHC and vHC have different efferent connectivity: the dHC projects to the mammillary bodies (MB), nucleus

accumbens (Trouche et al., 2019), anterior thalamic nuclei, and dorsolateral septum (DLS) nuclei, whereas the vHC sends monosynaptic projections to amygdala, nucleus accumbens, prefrontal cortex, hypothalamus, and DLS (Fanselow and Dong, 2010; Strange et al., 2014). Consequently, a fundamental question that arises is how information pertaining to certain and ambiguous contextual threats computed in the dHC and vHC is integrated and relayed to extrahippocampal circuits to calibrate fear responses. One mechanism is that information pertaining to certain and ambiguous threats computed in dHC and vHC is relayed to the amygdala, prefrontal cortex, and hypothalamus by vHC outputs. Alternatively, computations underlying certain and ambiguous threats are relayed directly out of the dHC and vHC through distinct pathways and integrated at extrahippocampal sites, such as the DLS (Besnard et al., 2019; Fanselow and Dong, 2010; Luo et al., 2011; Risold and Swanson, 1996) or thalamus (Fanselow and Dong, 2010; Liberzon and Abelson, 2016; Vertes, 2006; Xu and Südhof, 2013).

Within the HC, distinct subregions contribute differentially to encoding of contextual information. The dentate gyrus (DG)-CA3 circuit in dHC is thought to play a critical role in resolving overlapping contextual information to distinguish between certain and ambiguous threats (Besnard and Sahay, 2016; McHugh et al., 2007). At the neural level, this may be accomplished by pattern separation, a mechanism by which similar inputs are made divergent at the level of output (Berron et al., 2016; Besnard and Sahay, 2016; Deng et al., 2013; Lee et al., 2015; Leutgeb et al., 2007; Madar et al., 2019a, 2019b; McAvoy et al., 2016; Miller and Sahay, 2019; Neunuebel and Knierim, 2014; Sakon and Suzuki, 2019). Intriguingly, CA1 appears to be less sensitive to contextual discrimination and pattern separation, raising the question of how DG-CA3 computations resolving overlapping contextual information are propagated to extrahippocampal circuits without being modified or undone in CA1 (Knierim and Neunuebel, 2016; Leutgeb et al., 2004; Vazdarjanova and Guzowski, 2004; Yassa and Stark, 2011).

The DLS, a brain region comprised of a heterogeneous population of inhibitory neurons, by virtue of receiving direct hippocampal synaptic inputs, is ideally positioned to relay DG-CA3 computations resolving overlapping contextual information to the hypothalamus and the supramammillary nucleus (SUM) (McGlinchey and Aston-Jones, 2018; Pan and McNaughton, 2004; Risold and Swanson, 1996, 1997a, 1997b; Sheehan et al., 2004; Sweeney and Yang, 2015, 2016), a potent modulator of defensive behavior (Blanchard et al., 1998) (exploration, freezing), arousal, and stress responses (Campeau and Watson, 2000; Pan and McNaughton, 2004). We recently found that within the DLS, somatostatin (SST)-expressing neurons receive monosynaptic inputs from hippocampal CA3, CA1, and subiculum and these neurons gate mobility in aversive contexts (Besnard et al., 2019). Together, these observations suggest that contextual information may be relayed out of CA3 by CA1 or the DLS to cortical and subcortical circuits to calibrate fear responses.

Here, we used optogenetic terminal-specific attenuation to delineate the precise contributions of dorsal and ventral CA3 (vCA3) outputs to contextual fear discrimination learning (CFCDL). We found that optogenetic attenuation of excitatory dorsal CA3 (dCA3) projections to CA1 and DLS impaired behavioral fear responses (freezing levels) in conditioned and similar (neutral) contexts, respectively. In contrast, optogenetic attenuation

of excitatory vCA3 projections to CA1 and DLS had opposing effects on freezing behavior in both conditioned and similar, neutral contexts. Retrograde monosynaptic tracing, *ex vivo* electrophysiological recordings, and optogenetic manipulation identified DLS parvalbumin (PV) neurons as potential cellular relays of excitatory dCA3 outputs to proximal and distal subcortical circuits. Together, these studies illuminate how distinct dorsal and vCA3 outputs calibrate contextual fear discrimination.

RESULTS

Topographical Organization of Excitatory CA3/CA2 Projections in the DLS

We recently identified the CA3-DLS, but not the CA3-CA1 circuit, as highly sensitive to contextual fear discrimination (Besnard et al., 2019). Retrograde tracing studies have demonstrated that the DLS receives monosynaptic inputs from CA3, CA2, CA1, and the dorsal subiculum (Besnard et al., 2019; Leroy et al., 2018). In line with these previous findings, we observed robust CA3 excitatory projections to DLS in mice in which the Cre recombinase drives the expression of fluorescent genetic reporters (Ai27 and Ai35) in CA3 (Madisen et al., 2012; Nakazawa et al., 2002) (Figures 1A and 1B). Injection of rAAV5-CaMKII-ChR2-eYFP viral vectors into dCA3 or vCA3 of C57BL/6J mice (red arrows) illuminated topographically segregated projections in medial and lateral regions of DLS, respectively (Figures 1C and 1D), in addition to dorsal CA1 (dCA1) and ventral CA1 (vCA1) (red asterisks). These are most likely excitatory projections because viral labeling of GAD2-expressing cells (Taniguchi et al., 2011) in CA3 only illuminated projections to the medial septum (MS) (Figure 1E, asterisk). Collectively, these results suggest that dorsal and ventral CA3/CA2 excitatory projections are topographically organized along a mediolateral axis in the DLS, reminiscent of the pattern seen in the rat (Risold and Swanson, 1997b).

dCA3 Excitatory Projections to CA1 and DLS Mediate Fear Responses to Fearful and Neutral Contexts, Respectively

To evaluate the contributions of dCA3-dCA1 in processing certain (fear conditioning context A) and ambiguous contextual threats (similar, neutral context B) (Figure S1A), we used terminal-specific optogenetic attenuation using halorhodopsin during CFCDL (Figures 2A–2C). Optogenetic terminal-specific attenuation was performed after the training phase of CFCDL (or stabilization of discrimination learning performance) during block 7 in contexts A and B (Figures S1A–S1C). At the completion of CFCDL, mice were sacrificed at 30 or 60 min post-recall in context A or B for brain-wide c-Fos quantifications (Figures S1D, S1E, and S2). We performed bilateral injections of control rAAV5-CaMKIIa-eYFP or rAAV5-CaMKII-eNpHR3.0-eYFP (halorhodopsin) viral vectors into dCA3 of adult male C57BL/6J mice 3 weeks prior to stereotaxic implantation of fiber-optic probes above dCA1 (Figure S3A). Optogenetic attenuation of the dCA3-dCA1 pathway did not affect horizontal activity and behavioral measures of innate anxiety in the open-field (OF), elevated plus-maze (EPM), and novelty suppressed feeding (NSF) tests (Figures 2D–2G). Optogenetic attenuation of the dCA3-dCA1 pathway in block 7 preferentially decreased freezing behavior in context A (Figure 2H; Figures S3C and S3D) and resulted in a decrease in the discrimination ratio (Figure 2I). Analysis of brain-wide patterns of c-Fos expression following optogenetic attenuation of the dCA3-CA1 pathway 60 min post-exposure to

context A (Figure S3E) identified brain regions (Figure S4) in which c-Fos activity was either enhanced (e.g., MS, medial SUM, and dorsomedial periaqueductal gray [PAG]) or decreased (e.g., lateral amygdala [LA]) (Figure 2J; Figure S3I). These results suggest that dCA3-CA1 pathway recruits specific subcortical targets in response to contextual threat (context A).

To evaluate the contributions of dCA3-DLS in processing contextual fear discrimination, we used terminal-specific optogenetic attenuation using halorhodopsin during CFCDL (Figures 3A–3C). We performed bilateral injections of control rAAV5-CaMKIIa-eYFP or rAAV5-CamkII-eNpHR3.0-eYFP (halorhodopsin) viral vectors into dCA3 of adult male C57BL/6J mice 3 weeks prior to stereotaxic implantation of fiber-optic probes above DLS (Figure S3B). Optogenetic attenuation of the dCA3-DLS pathway did not affect horizontal activity and behavioral measures of innate anxiety in the OF, EPM, and NSF tests (Figures 3D–3G). Optogenetic attenuation of the dCA3-DLS pathway on block 7 preferentially decreased freezing behavior in context B (Figure 3H; Figures S3F and S3G), which resulted in an increase in the discrimination ratio (Figure 3I). Analysis of kinetics of c-Fos expression in DLS revealed significantly greater activation at 30 min than at 60 min post-exposure to context B (Figures S1E and S2G). We, therefore, analyzed brain-wide patterns of c-Fos expression following optogenetic attenuation of dCA3-DLS pathway at 30 min post-exposure to context B (Figure S3H). We identified brain regions in which c-Fos expression was either enhanced (e.g., lateral DLS, lateral hypothalamus [LH], and lateral PAG) or decreased (e.g., ventral BNST [bed nucleus of the stria terminalis] and dorsal DG) (Figure 3J; Figure S3J). These results suggest that the dCA3-DLS pathway recruits specific subcortical targets in response to ambiguous contextual threat (context B).

Together, these findings suggest that the dCA3-dCA1 and dCA3-DLS pathways are differentially required to mediate behavioral responses to certain and ambiguous contextual threats. Specifically, dCA3-dCA1 and dCA3-DLS pathways promote freezing behavior when the threat is certain or ambiguous, respectively.

The Strength of Contextual Fear Memory Determines the dCA3-DLS-Pathway-Dependent Calibration of Contextual Fear Discrimination

To determine whether dCA3-DLS-dependent modulation of freezing behavior in the neutral context necessitates encoding of the fear conditioned context, we assessed the impact of optogenetic attenuation of the dCA3-DLS pathway during early and late stages of CFCDL (Figure 3K). We performed bilateral injections of control rAAV5-CaMKIIa-eYFP or rAAV5-CamkII-eNpHR3.0-eYFP (halorhodopsin) viral vectors into dCA3 of adult male C57BL/6J mice 3 weeks prior to stereotaxic implantation of fiber-optic probes above DLS (Figure S5A). After an initial training session in context A on day 1, optogenetic terminal-specific attenuation was performed on day 2 in contexts A and B (counterbalanced) (Figure 3L). On day 2, optogenetic attenuation of dCA3-DLS terminals increased freezing behavior in context A but not context B (Figure 3M). After extended training in context A for 3 consecutive days (Figure 3N), optogenetic attenuation of the dCA3-DLS pathway decreased freezing behavior in context B but not context A (Figure 3O), reminiscent of what we had observed using an extended discrimination learning protocol (Figure 3H).

vCA3 Excitatory Projections to CA1 and DLS Exert Opposing Roles in Gating Contextual Fear Responses

To interrogate the roles of vCA3-vCA1 and vCA3-DLS pathways in processing certain (context A) and ambiguous contextual threats (context B), we used terminal-specific optogenetic attenuation using halorhodopsin during CFCDL as described above (Figures 4A–4C). We performed bilateral injections of control rAAV5-CaMKII α -eYFP or rAAV5-CaMKII α -eNpHR3.0-eYFP (halorhodopsin) viruses into vCA3 of adult male C57BL/6J mice 3 weeks prior to stereotaxic implantation of fiberoptic probes above vCA1 and DLS (Figures S6A and S6B). Optogenetic terminal-specific attenuation was performed after the training phase of CFCDL during block 7 in contexts A and B. Optogenetic attenuation of the vCA3-vCA1 pathway did not affect horizontal activity and behavioral measures of innate anxiety in the OF and EPM paradigms (Figures 4D–4F). However, a decrease in the latency to feed in the familiar but not novel context in the NSF test was observed (Figure 4G). In the CFCDL paradigm, both eYFP and eNpHR3.0 groups learned to discriminate between contexts A and B over the first 6 training blocks (Figure 4H). Optogenetic attenuation of vCA3-vCA1 terminals decreased overall freezing behavior in context A and B (Figure 4H, block 7; Figures S6C and S6D) without altering discrimination efficiency (Figure 4I).

Optogenetic attenuation of vCA3-DLS pathway (Figure 4J) did not affect horizontal activity and behavioral measures of innate anxiety in the OF and EPM paradigms (Figures 4K–4M). However, an increase in the latency to feed in the familiar but not novel context in the NSF test was observed (Figure 4N). Importantly, optogenetic attenuation of the vCA3-DLS pathway increased overall freezing levels (Figure 4O, block 7; Figures S6E and S6F) without altering discrimination specificity (Figure 4P). Note that in both vCA3-vCA1 and vCA3-DLS experiments, the effects on freezing behavior were dissociable from the change in freezing levels induced by tethering in block 7.

Optogenetic attenuation of the vCA3-DLS pathway dampened activity throughout the limbic brain, as assessed by c-Fos immunoreactivity 30 min following exposure to context B on day 21 (Figure S6G) (e.g., prelimbic [PL], DLS lateral, dorsal BNST, PVN [paraventricular nucleus], posterior CPuL [caudate putamen lateral], LA, BLA [basolateral amygdala], NAcc [nucleus accumbens] shell, and PAG) (Figure 4Q; Figure S6H). Collectively, these data suggest that the vCA3-vCA1 and vCA3-DLS pathways promote and decrease freezing levels, respectively, regardless of contextual fear certainty or ambiguity. Through their diametrically opposed roles, these two pathways may permit a coarse calibration of contextual fear responses.

vCA3 Excitatory Projections Modulate DLS SST Neuronal Activity

We have recently demonstrated that optogenetic silencing of SST-expressing neurons in DLS results in the enhancement of freezing behavior in a context nonspecific manner (Besnard et al., 2019). Here, we found that optogenetic attenuation of the vCA3-DLS pathway also results in the enhancement of freezing behavior in a context nonspecific manner (Figure 4O). To infer whether vCA3 projections recruit SST-expressing neurons to control freezing behavior, we measured c-Fos expression in SST neurons located in the lateral aspect of DLS following photosilencing of vCA3-DLS (Figure S7A) and vCA3-DLS (Figure S7D)

projections 30 min post-exposure to context B (Figures S3H and S6G). Optogenetic attenuation of vCA3 (Figures S7E and S7F) but not dCA3 (Figures S7B and S7C) inputs to DLS resulted in a decrease in c-Fos+SST+ neurons. These results suggest that vCA3 inputs to DLS may control defensive responses by recruiting SST-expressing neurons in DLS.

DLS PV Neurons Receive Monosynaptic Hippocampal Inputs and Send Long-Range Projections to Subcortical Circuits

Mapping of PV neuronal distribution in the DLS identified a sparse population of PV neurons localized within the dCA3 termination zone (Besnard et al., 2019). Histological examination of tdTomato-labeled PV neurons (PV-Cre::Ai14) confirmed preferential localization to the medial part of DLS (Figures 5A and 5B). All tdTomato-expressing cells in the DLS also expressed PV (data not shown). DLS PV neurons did not overlap with tdTomato-expressing cells in GAD2-Cre::Ai14 and SST-Cre::Ai14 mice (Figure 5C), suggesting that within the DLS, PV and SST neurons are non-overlapping cell populations. Finally, an analysis of overlap between PV immunostaining and tdTomato labeling in PV-Cre::Ai14 mice revealed that approximately 75% of DLS PV neurons underwent recombination (unlike the caudate putamen and nucleus accumbens) (Figure 5D).

To identify presynaptic partners of DLS PV neurons, we performed pseudotyped rabies virus *trans*-synaptic retrograde tracing (Sun et al., 2014; Wickersham et al., 2007). Infection with modified rabies virus (Env-A pseudotyped RABV [rabies virus] lacking G glycoprotein and expressing mCherry, SAD G-mCherry) is restricted to a specific, labeled population of starter cells expressing the avian receptor TVA (avian tumor virus receptor A) and limits tracing to first-order presynaptic partners, as further *trans*-synaptic spread is abrogated in the absence of glycoprotein. We bred PV-Cre mice with a conditional TVA-expressing mouse line (LSL-TVA) to generate PV-Cre::TVA mice (Seidler et al., 2008). We injected conditional AAV (adeno-associated virus) helper virus expressing GFP and EnvA-pseudotyped G-deleted rabies virus in DLS of PV-Cre::TVA mice, identified starter cells (GFP+mCherry+) in the DLS (Figure 5E, yellow arrowhead), and mapped the presynaptic cells (mCherry+) in the MS, diagonal band nucleus (DBN), dSubiculum, CA1, and CA3, albeit to a lesser extent (Figure 5F).

To establish whether CA3 projections functionally synapse onto PV-expressing neurons in DLS, we performed bilateral injections of control rAAV5-CamkII α -ChR2-eYFP (channelrhodopsin) virus into dCA3 of 4-week-old male PV-Cre::Ai14 mice and performed whole-cell patch clamp recordings in PV-expressing neurons (tdTomato-labeled) and non-PV cells (unlabeled) in DLS (Figure 5H). Light-evoked short latency (2 ± 0.7 ms) excitatory postsynaptic currents (eEPSCs) were detected in 35% of PV neurons (6/17 tdTomato-labeled cells from 4 mice) and 7% of non-PV neurons (2/27 unlabeled cells from 4 mice) following CA3 terminal activation by a single blue light pulse (5 ms, 0.1 Hz) (Figures 5I and 5J). In a subset of non-PV+ neurons, we observed a light-evoked delayed (46 ± 5 ms) inhibitory postsynaptic current (eIPSC) following a short latency (1.5 ± 0.8 ms) eEPSC, suggestive of feedforward inhibition (4/27 unlabeled cells) (Figures 5I and 5J). We compared the amplitude of excitatory currents of all light-responsive cells and found that inputs onto PV neurons were significantly larger than inputs onto non-PV neurons (Figure 5K). These data

demonstrate that PV-expressing neurons in DLS receive functional monosynaptic inputs from CA3.

An analysis of termination fields of DLS PV neurons revealed long-range projections to the DBN, lateral hypothalamus, and supramammillary nucleus (Figure 5L) that were largely overlapping with projections of SST-expressing DLS neurons (Besnard et al., 2019).

DLS PV Neurons Bidirectionally Regulate Contextual Fear Discrimination

To interrogate the role of PV neurons in contextual fear discrimination, we used cell-body-specific optogenetic silencing using halorhodopsin during CFCDL as described above (Figures 6A–6C). We performed bilateral injections of control rAAV5-DIO-eYFP or rAAV5-DIO-eNpHR3.0-eYFP (halorhodopsin) viruses into DLS of adult male PV-Cre mice 3 weeks prior to stereotaxic implantation of fiber optic probes above DLS (Figure S8A). Optogenetic silencing of DLS PV neurons did not affect horizontal activity and behavioral measures of innate anxiety in the OF, EPM, and NSF paradigms (Figures 6D–6G). In the CFCDL paradigm, both eYFP and eNpHR3.0 groups learned to discriminate between contexts A and B over the first 6 training blocks (Figure 6H). Optogenetic silencing of DLS PV neurons decreased freezing behavior only in context B (Figure 6H, block 7; Figures S8C and S8D), and this resulted in enhanced contextual fear discrimination (Figure 6I).

Optogenetic silencing of DLS PV neurons profoundly altered activity throughout the limbic brain, as assessed by c-Fos immunoreactivity 60 min following exposure to context B on day 21 (Figure S8E) (e.g., infralimbic [IL], NAcc shell, DLS lateral, BNST, posterior CPu, LA, PVT, SUM, and PAG) (Figure 6J; Figure S8I).

Next, we used cell-body-specific optogenetic stimulation using channelrhodopsin during CFCDL, as described above (Figures 7A–7C). We performed bilateral injections of control rAAV5-DIO-eYFP or rAAV5-DIO-ChR2-eYFP (channelrhodopsin) viral vectors into DLS of adult male PV-Cre mice 3 weeks prior to stereotaxic implantation of fiber optic probes above DLS (Figure S8B). Optogenetic stimulation (15 Hz) of DLS PV neurons did not affect horizontal activity and behavioral measures of innate anxiety in the OF and NSF paradigms (Figures 7D, 7E, and 7G) but exerted potent anxiolytic effects in the EPM (Figure 7F). In the CFCDL paradigm, both eYFP and ChR2 groups learned to discriminate between contexts A and B over the first 6 training blocks (Figure 7H). Optogenetic stimulation of DLS PV neurons altered freezing behavior levels in context A and B (Figure 7H, block 7; Figures S8F and S8G), and this resulted in decreased contextual fear discrimination (Figure 7I). Optogenetic stimulation of DLS PV neurons decreased activity throughout the limbic brain, as assessed by c-Fos immunoreactivity 60 min following exposure to context B on day 21 (Figure S8H) (e.g., IL, ventral BNST, PVN, PVT, dCA3, vCA1, and PAG lateral) (Figure 7J; Figure S8J). Collectively, these data suggest that DLS PV neurons may relay contextual information to downstream subcortical areas to calibrate fear responses in a context-specific manner.

DISCUSSION

A considerable body of work emphasizes a role for hippocampal-cortical and subcortical interactions in governing fear responses. However, the intra- and extrahippocampal pathways that route contextual information to cortical and subcortical circuits to guide adaptive behavioral responses are poorly understood. Here, we identified distinct contributions of dCA3 and vCA3 projections to CA1 and DLS in contextual fear discrimination and identified DLS PV and SST neurons as putative relays of dCA3 and vCA3 outputs in regulating fear responses to unequivocal and ambiguous contextual threats.

Consistent with a role for CA3 outputs in contextual memory consolidation (Nakashiba et al., 2008, 2009) and dCA3-dCA1 inputs in place field responses (Davoudi and Foster, 2019), we found that dCA3-dCA1 excitatory projections support recall of a fear conditioned context and, as such, mediate behavioral responses to certain contextual threats. In contrast, dCA3-DLS projections appear to be required for regulating freezing behavior in the similar neutral context once the memory of the training context is consolidated. That is, when mice are placed in the conditioned context and are immobile because of the certainty of threat, attenuation of excitatory CA3 projections to the DLS has no effect on freezing behavior (immobile to mobile state transition). In contrast, when mice are placed in the similar, neutral context, attenuation of excitatory CA3 projections to DLS decreases freezing levels.

Interestingly, we found that the dCA3-dCA1 pathway may dictate the engagement of the dCA3-DLS pathway to context discrimination. Specifically, we found that the strength of the contextual fear memory (presumably supported by dCA3-dCA1) determines dCA3-DLS-dependent modulation of freezing behavior in the neutral similar context. This is intuitive as contextual discrimination necessitates the proper encoding of the fear-conditioned context in the first place. Future work should investigate how contextual information is routed from dCA3 to dCA1 and DLS to govern contextual discrimination.

Our dCA3-DLS terminal-specific optogenetic silencing experiments warrant discussion of the physiological significance of weakening dCA3 outputs to the DLS. We speculate that efficient contextual discrimination in DG-CA3 is accompanied by the generation of a sparse code in CA3 (Knierim and Neunuebel, 2016; McAvoy et al., 2016; Neunuebel and Knierim, 2014; Niibori et al., 2012) that may arise from increased dentate granule cell recruitment of feedforward inhibition onto CA3 (Guo et al., 2018; Sun et al., 2017). This, in turn, results in weakening excitatory CA3 outputs to DLS to decrease freezing behavior in the similar neutral context. Interestingly, we have found that optogenetic attenuation of the dCA3-DLS pathway also promotes discrimination of social stimuli (Raam et al., 2017). Thus, discrimination of social and contextual information in DG-CA3 may attenuate the dCA3-DLS pathway to calibrate adaptive behavioral responses (reduced freezing in similar neutral context and increased social interaction).

In striking contrast to how context-specific information is routed by the dCA3-dCA1 and dCA3-DLS pathways, we found that vCA3-vCA1 and vCA3-DLS projections play a role in either promoting or decreasing defensive behavioral responses (freezing behavior) in a context-nonspecific manner. What functions might such circuit functional architecture

serve? One proposal is that the vCA3-vCA1-BLA and vCA3-DLS pathways may antagonistically recruit a common downstream target, such as the PAG, to calibrate fear responses (Tovote et al., 2016; Xu et al., 2016). The PAG may play a critical role in ultimately relaying subcortical inputs controlling active (dorsomedial and dorsolateral columns of PAG) and passive (lateral and ventrolateral columns of PAG) behavioral coping responses to threats (McNally et al., 2011). The antagonistic roles of vCA3-vCA1 and vCA3-DLS pathways may, therefore, enable vHC to provide a coarse calibration of fear responses despite inefficiently performing spatial pattern separation in ventral DG-CA3 (Kjelstrup et al., 2008; McAvoy et al., 2016).

Rabies tracing and optogenetic interrogation of DLS PV neurons suggest that these inhibitory neurons may relay dCA3 outputs to diverse subcortical circuits. Optogenetic inhibition of DLS PV neurons decreased freezing levels only in the similar neutral context, enhanced contextual fear discrimination, decreased c-Fos expression in the PAGdm (dorsomedial periaqueductal gray) and SUMm (medial supramammillary nucleus), and increased c-Fos expression in the LA. Conversely, silencing dCA3 projections to CA1 produced a decrease in freezing behavior in the context associated with footshock, decreased contextual fear discrimination, increased c-Fos expression in the PAGdm and SUMm, and decreased c-Fos expression in the LA. Although c-Fos expression analysis permits a first pass approximation of brain regions that may be directly or indirectly recruited by these different manipulations, changes in c-Fos may also reflect rebound and compensatory network effects (Mahn et al., 2016). Caveats notwithstanding, these results suggest that the calibration of freezing responses in the dangerous and ambiguous contexts, and therefore discrimination specificity, may differentially recruit CA3 projections to CA1 and DLS PV neurons to diametrically recruit PAG, SUM, and LA.

Recently, we found that optogenetic silencing of DLS SST neurons increased freezing behavior in a fear-conditioned context as well as a similar neutral context, which was associated with a decrease in c-Fos expression in PAGl (lateral periaqueductal gray), BLA, and PVN (Besnard et al., 2019). Here, we showed that optogenetic attenuation of vCA3-DLS terminals increased freezing behavior in the context associated with the footshock and the ambiguous context, and this manipulation was also associated with a decrease in c-Fos expression in the PAGl, BLA, and PVN. These data suggest that DLS PV and SST neurons may relay dCA3 and vCA3 outputs to calibrate fear responses by opposing recruitment of dorsal and lateral PAG. Further studies are needed to directly assess functional recruitment of these subcortical targets.

Together, these findings begin to illuminate how contextual information is routed by CA3 outputs along the hippocampal septotemporal axis to subcortical targets. A limitation of our study is that it does not distinguish between CA3 and CA2 subregions. Future efforts will refine contributions of CA1 and CA2 projections to DLS neurons in the calibration of defensive and motivated behaviors. Proximal and distal CA1 send projections to dorsal subiculum (Roy et al., 2017), whereas distal CA1 appears to preferentially target DLS PV neurons (present work). Simultaneous recordings of hippocampal subregions and their corresponding outputs may edify how different cognitive demands differentially recruit

specific efferent targets to generate adaptive behaviors (Bender et al., 2015; Ciocchi et al., 2015; Tingley and Buzsáki, 2018).

STAR★METHODS

KEY RESOURCES TABLE

REAGENT or RESOURCE	SOURCE	IDENTIFIER
Antibodies		
Rabbit polyclonal anti c-fos	Calbiochem	Cat# PC38, RRID: AB_2106755
Rabbit polyclonal anti c-fos	Santa Cruz	Cat# SC52, RRID: AB_2106783
Rabbit polyclonal anti-GFP	Life Technologies	Cat# A11122, RRID: AB_221569
Mouse monoclonal anti-PV	Millipore	Cat# MAB1572, RRID: AB_2174013
Goat polyclonal anti-SST	Santa Cruz	Cat# SC7819, RRID: AB_2302603
Alexa Fluor 488 donkey polyclonal anti-rabbit	Jackson ImmunoResearch	Cat#711-545-152, RRID: AB_2313584
Cy5 donkey polyclonal anti-rabbit	Jackson ImmunoResearch	Cat#711-175-152, RRID: AB_2340607
Alexa Fluor 647 donkey polyclonal anti-mouse	Jackson ImmunoResearch	Cat#715-605-151, RRID: AB_2340863
Cy3 donkey polyclonal anti-goat	Jackson ImmunoResearch	Cat#705-165-147, RRID: AB_2307351
Bacterial and Virus Strains		
AAV5-CaMKIIa-eYFP	UNC Vector Core	N/A
AAV5-CaMKIIa-eNpHR3.0-eYFP	UNC Vector Core	N/A
AAV5-CaMKIIa-hChr2(H134R)-eYFP	UNC Vector Core	N/A
AAV5-EF1a-DIO-eYFP-WPRE-hGH	UPENN Vector Core	Addgene27056
AAV5-EF1a-DIO-eNpHR3.0-WPRE-hGH	UPENN Vector Core	Addgene 26966
AAV5-EF1a-DIO-hChr2(H134R)-eYFP-WPRE-hGH	UPENN Vector Core	Addgene 20298P
AAV8- EF1a -FLEX-HB	Dr. Xiangmin Xu	N/A
Pseudotyped RG-deleted rabies virus EnvA-SAD G-mCherry	Dr. Xiangmiin Xu	N/A
Experimental Models: Organisms/Strains		
C57BL/6J <i>Mus musculus</i>	The Jackson Laboratory	RRID:IMSR_JAX:000664
C57BL/6-Tg(Grik4-cre)G32-4Std/J <i>Mus musculus</i>	The Jackson Laboratory	RRID:IMSR_JAX:006474
B6.Cg-Gt(ROSA)26Sortm27.1(CAG-COP4*H134R/tdTomato)Hze/J <i>Mus musculus</i>	The Jackson Laboratory	RRID:IMSR_JAX:012567
B6;129S-Gt(ROSA)26Sortm35.1(CAG-aop3/GFP)Hze/J <i>Mus musculus</i>	The Jackson Laboratory	RRID:IMSR_JAX:012735
B6J.Cg-Gad2tm2(cre)Zjh/MwarJ <i>Mus musculus</i>	The Jackson Laboratory	RRID:IMSR_JAX:028867
B6.129P2-Pvalbtm1(cre)Arbr/J <i>Mus musculus</i>	The Jackson Laboratory	RRID:IMSR_JAX:017320
B6J.Cg-Ssttm2.1(cre)Zjh/MwarJ <i>Mus musculus</i>	The Jackson Laboratory	RRID:IMSR_JAX:028864
B6.Cg-Gt(ROSA)26Sortm14(CAG-tdTomato)Hze/J <i>Mus musculus</i>	The Jackson Laboratory	RRID:IMSR_JAX:007914
Rosa-LSL-Tva-lacZ (mixed 129S6;C57BL/6J)	Dr. Dieter Saur	N/A
Software and Algorithms		

REAGENT or RESOURCE	SOURCE	IDENTIFIER
MotorMonitor	Kinder Scientific	http://kinderscientific.com
Videotrack	Viewpoint	http://www.viewpoint.fr/en/home
FreezeFrame	Actimetrics	https://www.actimetrics.com
FreezeView	Actimetrics	https://www.actimetrics.com
NIS Elements	Nikon	https://www.nikon.com
ImageJ	NIH	https://imagej.nih.gov/ij/
GraphPad Prism 7.0	GraphPad Software	https://www.graphpad.com/

LEAD CONTACT AND MATERIALS AVAILABILITY

All unique/stable reagents generated in this study are available from the Lead Contact without restriction. Further information and request for resources and reagents should be directed to and will be fulfilled by Amar Sahay (asahay@mgh.harvard.edu). This study did not generate new unique reagents.

EXPERIMENTAL MODEL AND SUBJECT DETAILS

Animal Care—Male mice were housed four per cage in a 12 hr (7:00 a.m. to 7:00 p.m.) light/dark colony room at 22°C–24°C with *ad libitum* access to food and water. Age-matched, male mice (3–4 months old) were used for behavioral experiments. Cagemates were pseudo-randomly assigned to groups during virus injection. Behavioral experiments took place between 8:00 a.m. and 6:00 p.m. All animals were handled and experiments were conducted in accordance with procedures approved by the Institutional Animal Care and Use Committee at the Massachusetts General Hospital and Boston University in accordance with NIH guidelines.

Mouse lines—8 week-old C57BL/6J male mice were purchased from Jackson labs (Bar Harbor, ME). G32–4 Cre mouse line expresses Cre recombinase primarily in CA3 pyramidal neurons expressing ionotropic kainate 4 glutamate receptor (Nakazawa et al., 2002). G32–4 Cre was purchased from Jackson labs (stock number 006474). Rosa-CAG-LSL-hChR2(H134R)-tdTomato-WPRE (Ai27) mouse line has a floxed-STOP cassette allowing transcription of ChR2-tdTomato fusion gene following Cre-mediated recombination (Madisen et al., 2012). Ai27 was purchased from Jackson labs (stock number 012567). Rosa-CAG-LSL-Arch-GFP-WPRE (Ai35) mouse line has a floxed-STOP cassette allowing transcription of Arch-GFP fusion gene following Cre-mediated recombination (Madisen et al., 2010). Ai35 was purchased from Jackson labs (stock number 012735). GAD2-IRES-Cre knock-in (C57BL/6J) mouse line expresses Cre-recombinase in GAD2-expressing neurons (Taniguchi et al., 2011). GAD2-IRES-Cre was purchased from Jackson labs (stock number 028867). PV-IRES-Cre knock in (C57BL/6J) mouse line expresses Cre recombinase in parvalbumin-expressing neurons (Hippenmeyer et al., 2005). PV-Cre was purchased from Jackson labs (stock number 017320). SST-IRES-Cre knock-in (C57BL/6J) mouse line expresses Cre recombinase in somatostatin-expressing neurons (Taniguchi et al., 2011). SST-IRES-Cre was purchased from Jackson labs (stock number 028864). Rosa-CAG-LSL-tdTomato-WPRE::deltaNeo (Ai14) (C57BL/6J) mouse line harbors a loxP-flanked STOP

cassette allowing transcription of CAG promoter-driven tdTomato following Cre-mediated recombination (Madisen et al., 2010). Ai14 was purchased from Jackson labs (stock number 007914). Rosa-LSL-Tva-lacZ (mixed 129S6;C57BL/6J) mouse line has a loxed-STOP cassette allowing transcription of avian receptor Tva-lacZ fusion gene following Cre-mediated recombination (Seidler et al., 2008). Rosa-LSL-TVA-lacZ mouse line was generously provided by Pr. Dieter Saur. Tail DNA from all offspring was genotyped by PCR to detect the presence of each transgene separately. All experiments were conducted with 8–16 week-old mice (unless indicated otherwise).

METHOD DETAILS

AAV Virus construction and packaging—The recombinant AAV5-CaMKII α -eYFP (6×10^{12} particles/mL), AAV5-CaMKII α -eNpHR3.0-eYFP (3×10^{12} particles/mL) and AAV5-CaMKII α -hChR2(H134R)-eYFP (4×10^{12} particles/mL), were packaged by the University of North Carolina Vector Core (Chapel Hill, NC). The recombinant AAV5-EF1a-DIO-eYFP-WPRE-hGH (5.8×10^{12} particles/mL), AAV5-EF1a-DIO-eNpHR3.0-WPRE-hGH (6×10^{12} particles/mL) and AAV5-EF1a-DIO-hChR2(H134R)-eYFP-WPRE-hGH (6.2×10^{12} particles/mL) were packaged by the University of Pennsylvania Vector Core (Philadelphia, PA). AAV8- EF1a -FLEX-HB (2×10^{11} particles/mL) and pseudotyped RG-deleted rabies virus EnvA-SAD G-mCherry (2×10^9 particles/mL) were kindly provided by Dr. Xiangmin Xu.

Viral Stereotactic surgery—Adult mice (8 week-old) were maintained under standard housing conditions, mice were given carprofen (5mg/kg, s.c., Patterson Veterinary Supply, Devens, MA) prior to surgery and 24h later to minimize discomfort. Mice were anaesthetized with ketamine and xylazine (10mg/mL and 1.6mg/mL, i.p, Patterson Veterinary Supply, Devens, MA) and placed in a stereotaxic frame (Stoelting, Holliston, MA). Small holes were drilled at each injection location and injected with a Hamilton microsyringe at a rate of 0.1 μ L/min. Viruses were injected into dorsal CA3 (+/- 2.5 mm ML, -2.1 mm AP, -2.25 mm DV from Bregma) of C57BL/6J mice (0.5 μ L, bilateral, 4 weeks for AAV5-CaMKII α -eYFP, ChR2 or eNpHR3.0) or GAD2-Cre mice (0.1 μ L, bilateral, 4 weeks for AAV5-EF1a-DIO-ChR2). Viruses were injected into ventral CA3 (+/- 3.0 mm ML, -3.25 mm AP, -4.0 mm DV from Bregma) of C57BL/6J mice (0.1 μ L, bilateral, 5 weeks for AAV5-CaMKII α -eYFP, ChR2 or eNpHR3.0). Viruses were injected into anterior dorsolateral septum (flat skull \pm 0.25 mm ML, +1.15 mm AP, -3 mm DV from Bregma) of PV-Cre mice (0.2 μ L, bilateral, 4weeks for AAV5-EF1a-DIO-eYFP, AAV5-EF1a-DIO-eNpHR3.0-eYFP or AAV5-EF1a-DIO-ChR2-eYFP). Viruses were injected into posterior dorsolateral septum (flat skull \pm 0.4 mm ML, +0.0 mm AP, -2.8 mm DV from Bregma) of PV-Cre::TVA mice (0.5 μ L, unilateral, 3weeks for AAV8- EF1a -FLEX-HB followed by 0.5 μ L, unilateral, 10 days for EnvA-SAD G-mCherry). After completion of the injection, the needle was left on the site of injection for 5 min, raised 0.2 mm and left on the site for an additional 5 min to allow diffusion of virus at the injection site and then slowly withdrawn. The skin incision was closed carefully using nylon sutures. Behavioral experiments were conducted 4–5 weeks following surgery (except for rabies tracing analysis which took place 10 days after EnvA-SAD G-mCherry infection).

Ex vivo electrophysiology—Two weeks post-viral injection, 6 weeks old mice were decapitated and coronal brain slices (250 μm thick) were prepared using a vibratome (VT1200S, Leica, Buffalo Grove, IL) in an ice slush NMDG solution containing (in mM): 92 NMDG, 2.5 KCl, 1.25 NaH_2PO_4 , 30 NaHCO_3 , 20 HEPES, 25 glucose, 2 thiourea, 5 Na-ascorbate, 3 Na-pyruvate, 0.5 CaCl_2 , 10 MgSO_4 , pH 7.3–7.4 (Ting et al., 2014). Slices recovered at 32°C in NMDG solution for 12 min and at room temperature for an additional 45 min in HEPES solution (in mM): 92 NaCl, 2.5 KCl, 1.25 NaH_2PO_4 , 30 NaHCO_3 , 20 HEPES, 25 glucose, 2 thiourea, 5 Na-ascorbate, 3 Na-pyruvate, 2 CaCl_2 , 2 MgSO_4 . All solutions were continually bubbled with O_2/CO_2 . During recordings, slices were kept at 32°C and continuously perfused at $\sim 2\text{ml}/\text{min}$ with aCSF (in mM): 126 NaCl, 2.5 KCl, 1.25 NaH_2PO_4 , 1.2 MgCl_2 , 10 glucose, 25 NaHCO_3 , 2 CaCl_2 . Whole-cell patch clamp recordings were made using Axopatch 700B amplifier (Molecular Devices), with Altering at 1 kHz using 4–6 $\text{M}\Omega$ electrodes filled with an internal solution containing (in mM): 130 K-gluconate, 10 HEPES, 5 NaCl, 1 EGTA, 5 Mg-ATP, 0.5 Na-GTP, pH 7.3, 280 mOsm. To induce light-evoked synaptic transmission, 5 ms blue light pulses (pE-100, Cool LED) were delivered through a 60X immersion objective centered above the recorded cell at a rate of 0.1 Hz. To measure excitatory responses, cells were held in voltage-clamp mode at -60 mV . For inhibitory evoked responses, cells were held in voltage-clamp mode at 0 mV . Responses were characterized as short latency if they occurred $< 5\text{ms}$ after termination of blue light stimulation, and delayed if they were $> 10\text{ ms}$ after blue light termination. Data acquisition was performed using Clampex and analyzed with Clampfit.

Construction of Optical Fibers—200 μm core, 0.37 numerical aperture (NA) multimode fiber (Thorlabs, Newton, NJ) was threaded through and glued with epoxy (Thorlabs, Newton, NJ) to a 230 μm core zirconia multimode ferrule (Precision Fiber Products, Milpitas, CA), polished and cut for implantation. Optical patch cables were generated the same way, with the free end connected to a multimode FC ferrule assembly for connecting to a 1 \times 2 Optical rotary joint (Doric lenses, Québec, Canada). The other end of the rotary joint was connected via a patch cable to 561 nm laser diode (OEM laser systems, Bluffdale, UT) via a non-contact style laser to fiber coupler (OZ optics, Ontario, Canada).

Fiber Optics Stereotactic surgery—Mice were surgically implanted with fiber optic cannulas 3 weeks following AAV5-CaMKII α -eYFP, AAV5-CaMKII α -eNpHR3.0-eYFP, AAV5-CaMKII α -hChR2(H134R)-eYFP, AAV5-EF1a-DIO-eYFP, AAV5-EF1a-DIO-eNpHR3.0-eYFP or AAV5-EF1a-DIO-ChR2-eYFP, injection and behavioral experiments started 1 week after surgery. Mice were implanted bilaterally with chronically dwelling optical fibers targeted to dorsolateral septum (flat skull $\pm 1.0\text{ mm}$ ML angle $\pm 10^\circ$, +1.15 mm AP from Bregma, implants length: 2.5 mm), dorsal CA1 ($\pm 1.5\text{ mm}$ ML, -2.0 mm AP from Bregma, implants length: 1.0 mm) and ventral CA1 ($\pm 3.65\text{ mm}$ ML, -3.05 mm AP from Bregma, implants length: 3.0 mm). Optical fibers were secured with dental cement. After surgery, mice were returned to their home cage and monitored until recovery from surgery.

In vivo Laser Delivery—Mice were kept in a quiet room for at least 1 h before testing. Behavioral tests took place under bright lighting conditions (700 lux) and performed in the

following order (Figures 1, 2, 3, 5, and 6): open field (day 1), elevated plus maze (day 2), novelty suppressed feeding (day 4) and contextual fear conditioning discrimination learning (CFCDL) (day 5–20). Abbreviated CFCDL experiment took place between day 1–6 (Figure 2). Prior to each experiment, mice were bilaterally attached to the patch cables via a zirconia sleeve (Precision Fiber Products, Milpitas, CA), and allowed to recover for 30–60 s in a transition cage similar to their home cage. The patch cables were interfaced to an FC/PC rotary joint (Doric lenses, Québec, Canada), which was attached on the other end to a 561 nm or 473 nm laser diode (OEM laser systems, Bluffdale, UT). The light power at the end of the fiber tip was 15–20 mW for 561 nm light and 8–10 mW for 473 nm light (5–6 mW when pulsing at 15 Hz). The laser diode was controlled by a Master-8 stimulator (Keysight Technology, Santa Clara, CA) which delivered 20 ms blue light pulses at 15 Hz. At the end of each behavioral experiment (5 to 7 weeks following viral surgery), post-mortem control of viral and fiber optics placement was carried out to ensure appropriate targeting.

Open field—Optogenetic interrogation of hippocampal circuits in the open field (OF) was recorded for 25 min divided in five 5 min laser epochs (OFF-ON-OFF-ON-OFF) in a Plexiglas open-field (OF) box of 41 × 41 cm with 16 sets of double stacked pulse-modulated infrared photobeams (Kinder Scientific, Poway, CA) equally spaced on every wall (128 total) to record x-y ambulatory movements. MotorMonitor Software (Kinder Scientific, Poway, CA) defined grid lines that divided the open field into center (25% of total area) and periphery (75% of total area), with the periphery consisting of the 10 cm closest to the wall around the entire perimeter. Dependent measures were the overall motor activity quantified as the total distance traveled (in centimeters) and the distance traveled in the center divided by total distance traveled (percentage distance in center). The apparatus was cleaned with 70% ethanol between each trial.

Elevated Plus Maze test—Optogenetic interrogation of hippocampal circuits in the elevated plus maze (EPM) was recorded for 15 min divided in three 5 min laser epochs (OFF-ON-OFF). The maze consisted of a black Plexiglas apparatus (Med Associates Inc., St. Albans, VT) placed 1 m above the floor, with two open arms (67 cm × 7 cm) perpendicular to two enclosed arms (67 × 7 × 17 cm). The four arms were separated by a neutral transition central square (5 × 5 cm) in which mice were placed at the beginning of the experiment and their behavior was recorded for 15 min with a video camera system (ViewPoint, Lyon, France) located above the maze. Cumulative time spent in the open and closed arms was scored manually by investigators blind to the treatment conditions and data were expressed as the time spent in open arms divided by total time in open and closed arms (percentage time in open arms). An arm visit was recorded when the mouse moved its forepaws into the arm. The apparatus was cleaned with 70% ethanol between each trial.

Novelty Suppressed Feeding test—Optogenetic interrogation of hippocampal circuits in the novelty suppressed feeding test (NSF) was recorded for up to 15 min in a novel context and up to 5 min in a familiar environment during which the laser was constantly ON. Mice were food deprived in clean home cages 24 hours prior to testing. Mice were weighed before food deprivation and again just before testing to assess changes in body weight (approximately 10% body weight loss). A single food pellet (familiar laboratory mouse

chow) was placed on a circular piece of white filter paper (12 cm diameter) positioned in the center of a plastic arena (45 cm wide × 30 cm long × 15 cm high) with wood chip bedding covering the floor. Mice were placed in a corner of the arena and the latency to approach the pellet and beginning feeding was recorded (maximum time 15 minutes). Immediately upon beginning to feed, each mouse was transferred to a familiar cage and the latency to begin feeding in the familiar cage was recorded (maximum time 5 minutes). Droppings were removed from the arena between each trial.

Contextual Fear conditioning Discrimination learning—The conditioning chambers (18 × 18 × 30 cm) consisted of 2 clear Plexiglas walls and ceiling, 2 metal walls, and a stainless steel grid floor (Coulbourn Instruments, Whitehall, PA). The conditioning chambers were placed inside a ventilated, sound-dampening isolation cubicles and lit by house lights mounted on one wall (Coulbourn Instruments, Whitehall, PA). FreezeFrame and FreezeView softwares (Actimetrics, Wilmette, IL) were used for recording and analyzing freezing behavior, respectively. For the training context (designated A throughout), the cubicle door was closed, the fan and house light were on, a light cue was on, stainless-steel bars were exposed, silver wall panels were used and each conditioning chamber was cleaned with 70% ethanol between each trial. Context B was a modified version of A by covering the stainless-steel bars with a solid floor covered with bedding, black wall panels were used (covering 30% of total wall surface), 15 cm high curved green plastic inserts covered the bottom half of the walls, and the house fan and lights were turned off. The cubicle door was left ajar and white noise was delivered through built-in speakers for the duration of the testing. The bedding was changed between trials. The contextual fear conditioning protocol consisted in delivering a single 2 s footshock of 0.7 mA, 180 s after placement of the mouse in the training context A. The mouse was taken out 20 s after termination of the footshock. No footshock was administered in context B during 180 s sessions. Mice were allowed to rest for 2–3 hours between tests. Freezing behavior over the initial 180 s was used to assess discrimination between both contexts. The discrimination ratio was calculated as (freezing in training context - freezing in similar context) / (freezing in training context + freezing in similar context). Figures 1, 2A–2J, 3,5, and 6: CFCDL consisted in 8 block (2 days each) trainings (days 5–20, untethered except for block 7). Two groups of mice (eYFP and eNpHR3.0 or eYFP and ChR2) were trained to discriminate between contexts A and B. Both contexts were presented once a day in a counterbalanced manner in order to avoid any session order bias. Block 7 was carried out with the laser constantly ON. On block 7, the percent time freezing as well as the number of freezing bouts and their average duration was measured. At the end of CFCDL, a final exposure to context B (day 21) with the laser ON took place 30 min or 60 min prior to sacrifice for c-Fos brain-wide analysis. A subset of eYFP and eNpHR3.0 mice (n = 2 per group randomly selected) was used for baseline c-Fos expression. Figures 2K–2O: After an initial training session in context A (day 1, tethered, no light), optogenetic terminal-specific silencing was performed on day 2 in contexts A and B with the laser constantly ON (counterbalanced for morning and afternoon session). A second phase of training took place in context A for 3 consecutive days (days 3–5, tethered, no light). On day 6, optogenetic terminal-specific silencing was performed in contexts A and B with the laser constantly ON (counterbalanced for morning and afternoon session).

Immunohistochemistry—Mice were anesthetized with ketamine and xylazine (100 and 3 mg/kg body weight, respectively) and transcardially perfused with PBS (10 mM phosphate buffer saline, pH 7.5,) at 4°C, followed by 4% paraformaldehyde in PBS at 4°C. Brains were post-fixed over-night in the same solution at 4°C, then cryoprotected in PBS sucrose (30% w/v) and stored at 4°C before freezing in OCT on dry ice. Coronal serial sections (35 µm) were obtained using a Leica cryostat in six matched sets. Sections were stored in PBS with 0.01% sodium azide at 4°C. On day 1, free-floating sections were rinsed three times for 10 min in 10 mM phosphate buffer saline (PBS), pH 7.5, followed by a permeabilization step 15 min in 0.2% Triton X-100 in PBS. The sections were rinsed another three times for 10 min in PBS and 2 h with a blocking buffer (10% natural donkey serum (NDS; w/v)). After three rinses in PBS, incubation with primary antibodies rabbit anti *c-fos*, Calbiochem PC38, 1:10,000 ([Antibodyregistry.org](https://antibodyregistry.org/AB_2106755): AB_2106755)(discontinued); different batches of rabbit, Santa Cruz SC52, 1:2,000–1:5,000 ([Antibodyregistry.org](https://antibodyregistry.org/AB_2106783): AB_2106783)(discontinued); rabbit anti-GFP, Life Technologies A11122, 1:500 ([Antibodyregistry.org](https://antibodyregistry.org/AB_221569): AB_221569); mouse anti-PV, Millipore MAB1572, 1:2,000 ([Antibodyregistry.org](https://antibodyregistry.org/AB_2174013): AB_2174013); goat anti-SST, Santa Cruz SC7819, 1:400 ([Antibodyregistry.org](https://antibodyregistry.org/AB_2302603): AB_2302603)(discontinued) was carried out with shaking at 4°C overnight. On day 2, sections were rinsed three times for 10 min in PBS and incubated for 90 min with a donkey anti-rabbit, anti-mouse and/or anti-goat Alexa Fluor 488-, Alexa Fluor 647-, Cy3-, or Cy5-coupled secondary antibody (Jackson ImmunoResearch, 1:500). Sections were rinsed three times for 10 min in PBS before mounting in PBS and coverslipped with Fluoromount.

Images acquisition and analysis—Images were obtained from one set of brain sections (1/6th of the brain) for each immunostaining. For single stainings (*c-Fos* or GFP), brain regions of interest were identified at various Bregma coordinates. Images were acquired bilaterally with an epifluorescence microscope (Nikon) using a 10× objective. High-resolution reconstruction was achieved by combining multiple images with overlapping fields of view (NIS Elements software). Quantifications were performed manually using an image analysis software (ImageJ 1.49v, NIH), taking into account cells with immunofluorescence above background. For dual immunostainings (PV co-labeled with tdTomato, GFP co-labeled with mCherry, *c-Fos* co-labeled with SST), z stacks images were acquired bilaterally with a Nikon A1R Si confocal laser, a TiE inverted research microscope using a 20× objective. Images (1024 resolution) were acquired as 14 µM z stacks with a step size of 2 µM. For *c-Fos* intensity in SST cells (Figure S7), we measured *c-Fos* immunoreactivity in SST cells and expressed the data as a percentage of background in the same field of view. All analyses were performed by an investigator blinded to treatment and/or genotype.

QUANTIFICATION AND STATISTICAL ANALYSIS

Scoring—During testing, investigators were not blind to conditions. However, results were replicated across several cohorts. Videos for behavioral scoring (i.e., freezing behavior) were analyzed using FreezeView softwares (Actimetrics, Wilmette, IL) during sessions without light application. For sessions in which mice received photostimulation (or silencing), the light coming out of the implants prevented automatic scoring and was therefore independently scored by 2 investigators. Other analyses of behavior such as ambulation in

the open-field was scored automatically using MotorMonitor Software (Kinder Scientific, Poway, CA). Anxiety assessment in the elevated plus maze and novelty suppressed feeding tests were carried out by 1 investigator blinded to treatment and/or genotype. Sahay (PI) selected individuals in the lab to perform independent scoring.

Statistical Analysis—No statistical methods were used to pre-determine sample sizes but our sample sizes are similar to those reported in previous publications (Felix-Ortiz et al., 2013; Xu et al., 2016). Statistical analysis was carried out using GraphPad Prism v7 software. Data (means \pm SEM) were analyzed using paired or unpaired two-tailed Student's t test, ordinary one-way ANOVA followed by Tukey's multiple comparisons test when appropriate (difference among means, $p < 0.05$), mixed factor two-way ANOVA (repeated-measures over time) followed by Bonferroni's multiple comparisons test when appropriate (only if interaction, $p < 0.05$). Multiple comparisons for correlation matrix data were corrected with Bonferroni's correction method. Novelty suppressed feeding data were analyzed using Log-Rank (Mantel Cox) test. Data distribution was assumed to be normal but this was not formally tested unless specified otherwise. Detailed statistical analyses can be found in Table S1. In any case, significance was set at $p < 0.05$.

Data exclusion—Figures 4J–4P consisted of two cohorts of eYFP ($n = 8$) and eNpHR3.0 ($n = 12$), among which 2 eYFP mice lost their fiber optic implants because of handling, total number of animals eYFP ($n = 14$) and eNpHR3.0 ($n = 24$). Figure 5 consisted of 5 cohorts of 4 PV-Cre::TVA mice ($n = 20$). Because of the sparse distribution of PV neurons in DLS, very few mice ($n = 2$) displayed enough starter cells to perform relevant brain-wide quantifications of presynaptic partners. Figure 7 consisted of one cohort of DIO-eYFP ($n = 8$) and DIO-ChR2 ($n = 8$) among which 2 DIO-ChR2 mice were excluded based on their mis-targeted fiber optic implants.

DATA AND CODE AVAILABILITY

All data generated in this study are available from the Lead Contact without restriction. Further information and request for original data should be directed to and will be fulfilled by Amar Sahay (asahay@mg.harvard.edu).

Supplementary Material

Refer to Web version on PubMed Central for supplementary material.

ACKNOWLEDGMENTS

We wish to thank members of the Sahay lab for their comments on the manuscript. A.B. is supported by 2014 NARSAD Young Investigator Award, Bettencourt Schueller Foundation, Philippe Foundation, and 2016 MGH ECOR Fund for Medical Discovery (FMD) Postdoctoral Fellowship Awards. A.S. acknowledges support from NIH-R01MH104175, NIH-R01AG048908, and NIH-1R01MH111729; James and Audrey Foster MGH Research Scholar Award; the Ellison Medical Foundation New Scholar in Aging; the Whitehall Foundation; an Inscopix Decode award; a NARSAD Independent Investigator Award; Ellison Family Philanthropic support; the Blue Guitar Fund; a Harvard Neurodiscovery Center–MADRC Center Pilot Grant award; Alzheimer's Association Research Grant; a Harvard Stem Cell Institute Development grant; and a HSCI seed grant.

REFERENCES

- Bannerman DM, Sprengel R, Sanderson DJ, McHugh SB, Rawlins JN, Monyer H, and Seeburg PH (2014). Hippocampal synaptic plasticity, spatial memory and anxiety. *Nat. Rev. Neurosci* 15, 181–192. [PubMed: 24552786]
- Bender F, Gorbati M, Cadavieco MC, Denisova N, Gao X, Holman C, Korotkova T, and Ponomarenko A (2015). Theta oscillations regulate the speed of locomotion via a hippocampus to lateral septum pathway. *Nat. Commun* 6, 8521. [PubMed: 26455912]
- Berron D, Schütze H, Maass A, Cardenas-Blanco A, Kuijf HJ, Kumaran D, and Düzel E (2016). Strong Evidence for Pattern Separation in Human Dentate Gyrus. *J. Neurosci* 36, 7569–7579. [PubMed: 27445136]
- Besnard A, and Sahay A (2016). Adult Hippocampal Neurogenesis, Fear Generalization, and Stress. *Neuropsychopharmacology* 41, 24–44. [PubMed: 26068726]
- Besnard A, Gao Y, TaeWoo Kim M, Twarkowski H, Reed AK, Langberg T, Feng W, Xu X, Saur D, Zweifel LS, et al. (2019). Dorsolateral septum somatostatin interneurons gate mobility to calibrate context-specific behavioral fear responses. *Nat. Neurosci* 22, 436–446. [PubMed: 30718902]
- Blanchard RJ, Hebert MA, Ferrari PF, Palanza P, Figueira R, Blanchard DC, and Parmigiani S (1998). Defensive behaviors in wild and laboratory (Swiss) mice: the mouse defense test battery. *Physiol. Behav* 65, 201–209. [PubMed: 9855467]
- Campeau S, and Watson SJ Jr. (2000). Connections of some auditory-responsive posterior thalamic nuclei putatively involved in activation of the hypothalamo-pituitary-adrenocortical axis in response to audiogenic stress in rats: an anterograde and retrograde tract tracing study combined with Fos expression. *J. Comp. Neurol* 423, 474–491. [PubMed: 10870087]
- Ciocchi S, Passecker J, Malagon-Vina H, Mikus N, and Klausberger T (2015). Brain computation. Selective information routing by ventral hippocampal CA1 projection neurons. *Science* 348, 560–563. [PubMed: 25931556]
- Davoudi H, and Foster DJ (2019). Acute silencing of hippocampal CA3 reveals a dominant role in place field responses. *Nat. Neurosci* 22, 337–342. [PubMed: 30664772]
- Deng W, Mayford M, and Gage FH (2013). Selection of distinct populations of dentate granule cells in response to inputs as a mechanism for pattern separation in mice. *eLife* 2, e00312. [PubMed: 23538967]
- Fanselow MS, and Dong HW (2010). Are the dorsal and ventral hippocampus functionally distinct structures? *Neuron* 65, 7–19. [PubMed: 20152109]
- Felix-Ortiz AC, Beyeler A, Seo C, Leppla CA, Wildes CP, and Tye KM (2013). BLA to vHPC inputs modulate anxiety-related behaviors. *Neuron* 79, 658–664. [PubMed: 23972595]
- Frankland PW, Cestari V, Filipkowski RK, McDonald RJ, and Silva AJ (1998). The dorsal hippocampus is essential for context discrimination but not for contextual conditioning. *Behav. Neurosci* 112, 863–874. [PubMed: 9733192]
- Guo N, Soden ME, Herber C, Kim MT, Besnard A, Lin P, Ma X, Cepko CL, Zweifel LS, and Sahay A (2018). Dentate granule cell recruitment of feedforward inhibition governs engram maintenance and remote memory generalization. *Nat. Med* 24, 438–449. [PubMed: 29529016]
- Hippenmeyer S, Vrieseling E, Sigrist M, Portmann T, Laengle C, Ladle DR, and Arber S (2005). A developmental switch in the response of DRG neurons to ETS transcription factor signaling. *PLoS Biol.* 3, e159. [PubMed: 15836427]
- Jimenez JC, Su K, Goldberg AR, Luna VM, Biane JS, Ordek G, Zhou P, Ong SK, Wright MA, Zweifel L, et al. (2018). Anxiety Cells in a Hippocampal-Hypothalamic Circuit. *Neuron* 97, 670–683. e676. [PubMed: 29397273]
- Kheirbek MA, Drew LJ, Burghardt NS, Costantini DO, Tannenholz L, Ahmari SE, Zeng H, Fenton AA, and Hen R (2013). Differential control of learning and anxiety along the dorsoventral axis of the dentate gyrus. *Neuron* 77, 955–968. [PubMed: 23473324]
- Kim JJ, and Fanselow MS (1992). Modality-specific retrograde amnesia of fear. *Science* 256, 675–677. [PubMed: 1585183]

- Kjelstrup KB, Solstad T, Brun VH, Hafting T, Leutgeb S, Witter MP, Moser EI, and Moser MB (2008). Finite scale of spatial representation in the hippocampus. *Science* 321, 140–143. [PubMed: 18599792]
- Knierim JJ, and Neunuebel JP (2016). Tracking the flow of hippocampal computation: Pattern separation, pattern completion, and attractor dynamics. *Neurobiol. Learn. Mem* 129, 38–49. [PubMed: 26514299]
- Lee H, Wang C, Deshmukh SS, and Knierim JJ (2015). Neural Population Evidence of Functional Heterogeneity along the CA3 Transverse Axis: Pattern Completion versus Pattern Separation. *Neuron* 87, 1093–1105. [PubMed: 26298276]
- Leroy F, Park J, Asok A, Brann DH, Meira T, Boyle LM, Buss EW, Kandel ER, and Siegelbaum SA (2018). A circuit from hippocampal CA2 to lateral septum disinhibits social aggression. *Nature* 564, 213–218. [PubMed: 30518859]
- Leutgeb S, Leutgeb JK, Treves A, Moser MB, and Moser EI (2004). Distinct ensemble codes in hippocampal areas CA3 and CA1. *Science* 305, 1295–1298. [PubMed: 15272123]
- Leutgeb JK, Leutgeb S, Moser MB, and Moser EI (2007). Pattern separation in the dentate gyrus and CA3 of the hippocampus. *Science* 315, 961–966. [PubMed: 17303747]
- Liberzon I, and Abelson JL (2016). Context Processing and the Neurobiology of Post-Traumatic Stress Disorder. *Neuron* 92, 14–30. [PubMed: 27710783]
- Luo AH, Tahsili-Fahadan P, Wise RA, Lupica CR, and Aston-Jones G (2011). Linking context with reward: a functional circuit from hippocampal CA3 to ventral tegmental area. *Science* 333, 353–357. [PubMed: 21764750]
- Madar AD, Ewell LA, and Jones MV (2019a). Pattern separation of spike-trains in hippocampal neurons. *Sci. Rep* 9, 5282. [PubMed: 30918288]
- Madar AD, Ewell LA, and Jones MV (2019b). Temporal pattern separation in hippocampal neurons through multiplexed neural codes. *PLoS Comput. Biol* 15,e1006932. [PubMed: 31009459]
- Madisen L, Zwingman TA, Sunkin SM, Oh SW, Zariwala HA, Gu H, Ng LL, Palmiter RD, Hawrylycz MJ, Jones AR, et al. (2010). A robust and high-throughput Cre reporting and characterization system for the whole mouse brain. *Nat. Neurosci* 13, 133–140. [PubMed: 20023653]
- Madisen L, Mao T, Koch H, Zhuo JM, Berenyi A, Fujisawa S, Hsu YW, Garcia AJ 3rd, Gu X, Zanella S, et al. (2012). A toolbox of Cre-dependent optogenetic transgenic mice for light-induced activation and silencing. *Nat. Neurosci* 15, 793–802. [PubMed: 22446880]
- Mahn M, Prigge M, Ron S, Levy R, and Yizhar O (2016). Biophysical constraints of optogenetic inhibition at presynaptic terminals. *Nat. Neurosci* 19, 554–556. [PubMed: 26950004]
- Maren S, Phan KL, and Liberzon I (2013). The contextual brain: implications for fear conditioning, extinction and psychopathology. *Nat. Rev. Neurosci* 14, 417–428. [PubMed: 23635870]
- McAvoy KM, Scobie KN, Berger S, Russo C, Guo N, Decharatanachart P, Vega-Ramirez H, Miake-Lye S, Whalen M, Nelson M, et al. (2016). Modulating Neuronal Competition Dynamics in the Dentate Gyrus to Rejuvenate Aging Memory Circuits. *Neuron* 91, 1356–1373. [PubMed: 27593178]
- McGlinchey EM, and Aston-Jones G (2018). Dorsal Hippocampus Drives Context-Induced Cocaine Seeking via Inputs to Lateral Septum. *Neuropsychopharmacology* 43, 987–1000. [PubMed: 28695893]
- McHugh TJ, Jones MW, Quinn JJ, Balthasar N, Coppari R, Elmquist JK, Lowell BB, Fanselow MS, Wilson MA, and Tonegawa S (2007). Dentate gyrus NMDA receptors mediate rapid pattern separation in the hippocampal network. *Science* 317, 94–99. [PubMed: 17556551]
- McNally GP, Johansen JP, and Blair HT (2011). Placing prediction into the fear circuit. *Trends Neurosci.* 34, 283–292. [PubMed: 21549434]
- Miller SM, and Sahay A (2019). Functions of adult-born neurons in hippocampal memory interference and indexing. *Nat. Neurosci* 22, 1565–1575. [PubMed: 31477897]
- Nakashiba T, Young JZ, McHugh TJ, Buhl DL, and Tonegawa S (2008). Transgenic inhibition of synaptic transmission reveals role of CA3 output in hippocampal learning. *Science* 319, 1260–1264. [PubMed: 18218862]

- Nakashiba T, Buhl DL, McHugh TJ, and Tonegawa S (2009). Hippocampal CA3 output is crucial for ripple-associated reactivation and consolidation of memory. *Neuron* 62, 781–787. [PubMed: 19555647]
- Nakazawa K, Quirk MC, Chitwood RA, Watanabe M, Yeckel MF, Sun LD, Kato A, Carr CA, Johnston D, Wilson MA, and Tonegawa S (2002). Requirement for hippocampal CA3 NMDA receptors in associative memory recall. *Science* 297, 211–218. [PubMed: 12040087]
- Neunuebel JP, and Knierim JJ (2014). CA3 retrieves coherent representations from degraded input: direct evidence for CA3 pattern completion and dentate gyrus pattern separation. *Neuron* 81, 416–427. [PubMed: 24462102]
- Niibori Y, Yu TS, Epp JR, Akers KG, Josselyn SA, and Frankland PW (2012). Suppression of adult neurogenesis impairs population coding of similar contexts in hippocampal CA3 region. *Nat. Commun* 3, 1253. [PubMed: 23212382]
- Pan WX, and McNaughton N (2004). The supramammillary area: its organization, functions and relationship to the hippocampus. *Prog. Neurobiol* 74, 127–166. [PubMed: 15556285]
- Raam T, McAvoy KM, Besnard A, Veenema AH, and Sahay A (2017). Hippocampal oxytocin receptors are necessary for discrimination of social stimuli. *Nat. Commun* 8, 2001. [PubMed: 29222469]
- Risold PY, and Swanson LW (1996). Structural evidence for functional domains in the rat hippocampus. *Science* 272, 1484–1486. [PubMed: 8633241]
- Risold PY, and Swanson LW (1997a). Chemoarchitecture of the rat lateral septal nucleus. *Brain Res. Brain Res. Rev* 24, 91–113. [PubMed: 9385453]
- Risold PY, and Swanson LW (1997b). Connections of the rat lateral septal complex. *Brain Res. Brain Res. Rev* 24, 115–195. [PubMed: 9385454]
- Roy DS, Kitamura T, Okuyama T, Ogawa SK, Sun C, Obata Y, Yoshiki A, and Tonegawa S (2017). Distinct Neural Circuits for the Formation and Retrieval of Episodic Memories. *Cell* 170, 1000–1012.e1019. [PubMed: 28823555]
- Sakon JJ, and Suzuki WA (2019). A neural signature of pattern separation in the monkey hippocampus. *Proc. Natl. Acad. Sci. USA* 116, 9634–9643. [PubMed: 31010929]
- Seidler B, Schmidt A, Mayr U, Nakhai H, Schmid RM, Schneider G, and Saur D (2008). A Cre-loxP-based mouse model for conditional somatic gene expression and knockdown in vivo by using avian retroviral vectors. *Proc. Natl. Acad. Sci. USA* 105, 10137–10142. [PubMed: 18621715]
- Sheehan TP, Chambers RA, and Russell DS (2004). Regulation of affect by the lateral septum: implications for neuropsychiatry. *Brain Res. Brain Res. Rev* 46, 71–117. [PubMed: 15297155]
- Strange BA, Witter MP, Lein ES, and Moser EI (2014). Functional organization of the hippocampal longitudinal axis. *Nat. Rev. Neurosci* 15, 655–669. [PubMed: 25234264]
- Sun Y, Nguyen AQ, Nguyen JP, Le L, Saur D, Choi J, Callaway EM, and Xu X (2014). Cell-type-specific circuit connectivity of hippocampal CA1 revealed through Cre-dependent rabies tracing. *Cell Rep.* 7, 269–280. [PubMed: 24656815]
- Sun Q, Sotayo A, Cazzulino AS, Snyder AM, Denny CA, and Siegelbaum SA (2017). Proximodistal Heterogeneity of Hippocampal CA3 Pyramidal Neuron Intrinsic Properties, Connectivity, and Reactivation during Memory Recall. *Neuron* 95, 656–672.e653. [PubMed: 28772124]
- Sweeney P, and Yang Y (2015). An excitatory ventral hippocampus to lateral septum circuit that suppresses feeding. *Nat. Commun* 6, 10188. [PubMed: 26666960]
- Sweeney P, and Yang Y (2016). An Inhibitory Septum to Lateral Hypothalamus Circuit That Suppresses Feeding. *J. Neurosci* 36, 11185–11195. [PubMed: 27807162]
- Taniguchi H, He M, Wu P, Kim S, Paik R, Sugino K, Kvitsiani D, Fu Y, Lu J, Lin Y, et al. (2011). A resource of Cre driver lines for genetic targeting of GABAergic neurons in cerebral cortex. *Neuron* 71, 995–1013. [PubMed: 21943598]
- Ting JT, Daigle TL, Chen Q, and Feng G (2014). Acute brain slice methods for adult and aging animals: application of targeted patch clamp analysis and optogenetics. *Methods Mol. Biol* 1183, 221–242. [PubMed: 25023312]
- Tingley D, and Buzsáki G (2018). Transformation of a Spatial Map across the Hippocampal-Lateral Septal Circuit. *Neuron* 98, 1229–1242.e5. [PubMed: 29779942]

- Tovote P, Esposito MS, Botta P, Chaudun F, Fadok JP, Markovic M, Wolff SB, Ramakrishnan C, Fenno L, Deisseroth K, et al. (2016). Midbrain circuits for defensive behaviour. *Nature* 534, 206–212. [PubMed: 27279213]
- Trouche S, Koren V, Doig NM, Ellender TJ, El-Gaby M, Lopes-Dos-Santos V, Reeve HM, Perestenko PV, Garas FN, Magill PJ, et al. (2019). A Hippocampus-Accumbens Tripartite Neuronal Motif Guides Appetitive Memory in Space. *Cell* 176, 1393–1406.e1316. [PubMed: 30773318]
- Vazdarjanova A, and Guzowski JF (2004). Differences in hippocampal neuronal population responses to modifications of an environmental context: evidence for distinct, yet complementary, functions of CA3 and CA1 ensembles. *J. Neurosci* 24, 6489–6496. [PubMed: 15269259]
- Vertes RP (2006). Interactions among the medial prefrontal cortex, hippocampus and midline thalamus in emotional and cognitive processing in the rat. *Neuroscience* 142, 1–20. [PubMed: 16887277]
- Wickersham IR, Finke S, Conzelmann KK, and Callaway EM (2007). Retrograde neuronal tracing with a deletion-mutant rabies virus. *Nat. Methods* 4, 47–49. [PubMed: 17179932]
- Xu W, and Südhof TC (2013). A neural circuit for memory specificity and generalization. *Science* 339, 1290–1295. [PubMed: 23493706]
- Xu C, Krabbe S, Grundemann J, Botta P, Fadok JP, Osakada F, Saur D, Grewe BF, Schnitzer MJ, Callaway EM, et al. (2016). Distinct Hippocampal Pathways Mediate Dissociable Roles of Context in Memory Retrieval. *Cell* 167, 961–972.e916. [PubMed: 27773481]
- Yassa MA, and Stark CE (2011). Pattern separation in the hippocampus. *Trends Neurosci.* 34, 515–525. [PubMed: 21788086]

Highlights

- CA3 projections to CA1 and dorsolateral septum (DLS) contribute to contextual fear
- Dorsal CA3-CA1 and CA3-DLS projections mediate context-specific defensive responses
- Ventral CA3-CA1 and vCA3-DLS projections play opposing roles in defensive responses
- DLS-PV neurons mediate context-specific defensive responses

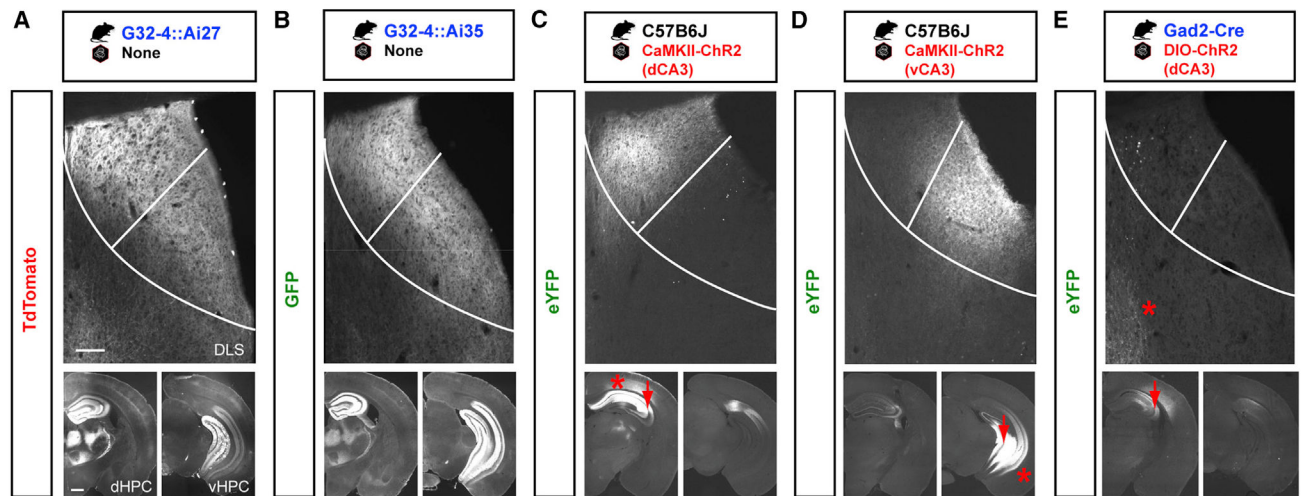


Figure 1. Topographical Organization of Excitatory CA3 Projections in DLS

(A and B) Forward mapping of CA3 excitatory terminals in DLS obtained from the progeny of G32–4 bred with Ai27 (tdTomato) or Ai35 (GFP). In these mouse lines, ChR2-tdTomato or Arch-GFP is restricted mainly to CA3 (bottom panels). Note the abundance of terminals in DLS (top panels).

(C and D) Local injection of CaMKII-ChR2-eYFP in dorsal or ventral CA3 of C57B6/J mice leads to restricted expression of eYFP in the medial or lateral part of DLS, respectively. Asterisks denote the abundance of terminals in dorsal and ventral CA1, respectively.

(E) Dorsal CA3 inhibitory neurons do not innervate DLS, as evidenced by selective infection of GAD2-Cre mice with DIO-ChR2-eYFP. Asterisk denotes the presence of terminals in the medial septum. Scale bar: 100 μ m.

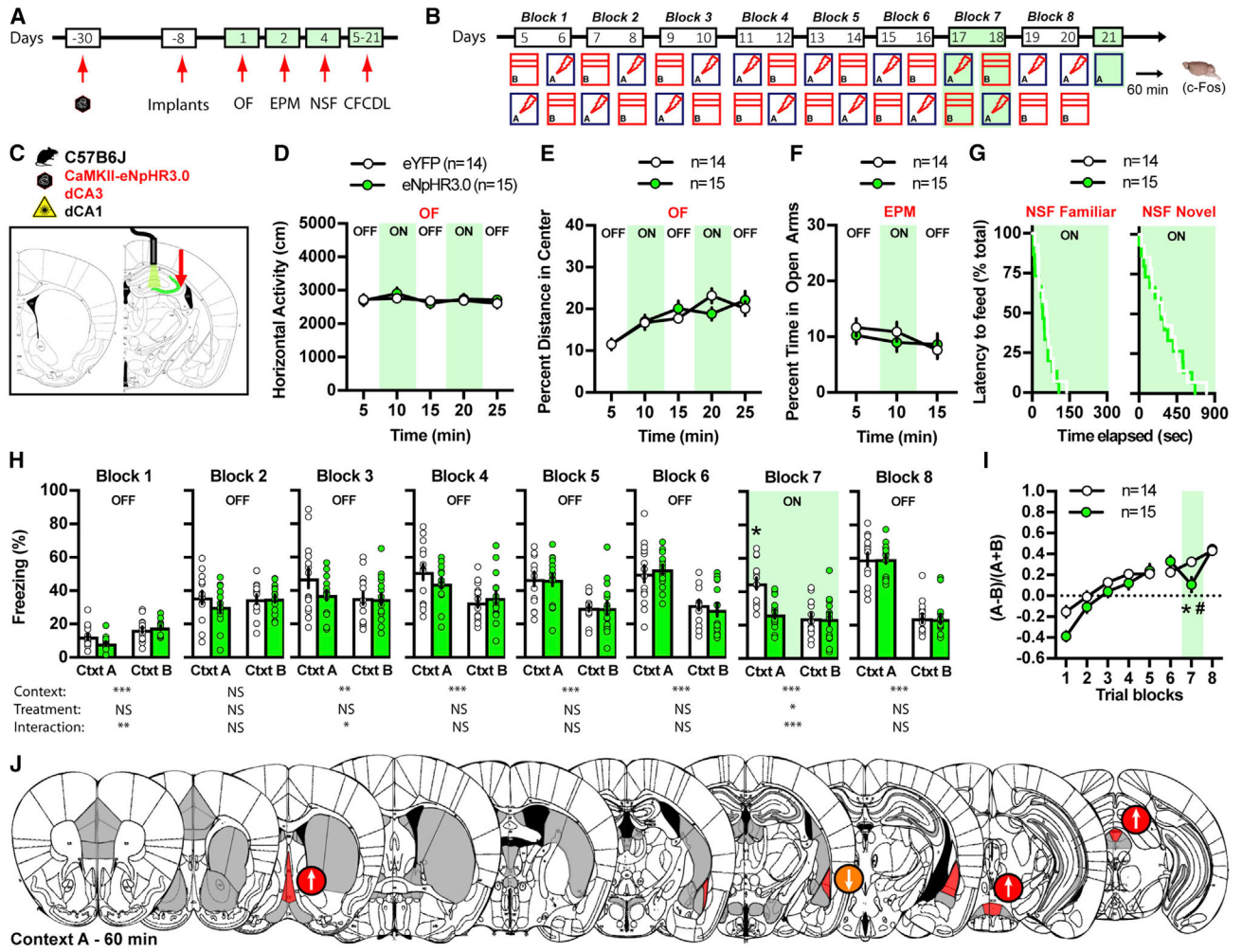


Figure 2. Dorsal CA3 Excitatory Projections to CA1 Instruct Fear Responses to Certain but Not Ambiguous Contextual Threats

(A and B) Schematic of the behavioral timeline.

(C) Schematic illustrating dorsal CA3 infection with CaMKII-eNpHR3.0 and fiber optic implantation on top of dorsal CA1 in C57B6/J mice.

(D–G) Silencing dorsal CA3 terminals in dorsal CA1 has no effect on locomotor behavior and innate anxiety in OF (D and E), EPM (F), and NSF (G).

(H and I) Silencing dorsal CA3 terminals in dorsal CA1 decreases freezing behavior in context A but not B (H), which results in a decrease in fear discrimination ratio on block 7 (I). Data (means ± SEM; n = 14, 15 mice per group) were analyzed using mixed factor two-way ANOVA (repeated measure over time) followed by Bonferroni’s multiple comparisons post hoc test and log-rank (Mantel Cox) test. *p < 0.05, eNpHR3.0 versus eYFP; #p < 0.05, block 7 versus block 6. Statistics detailed in Table S1.

(J) Schematic representation of the effect of light silencing dorsal CA3 terminals in CA1 on brain-wide c-Fos expression 60 min following exposure to context A (day 21). Regions highlighted in red denote a significant effect of eNpHR3.0, and arrows indicate the direction of the effect.

See also Figures S1, S3, and S4.

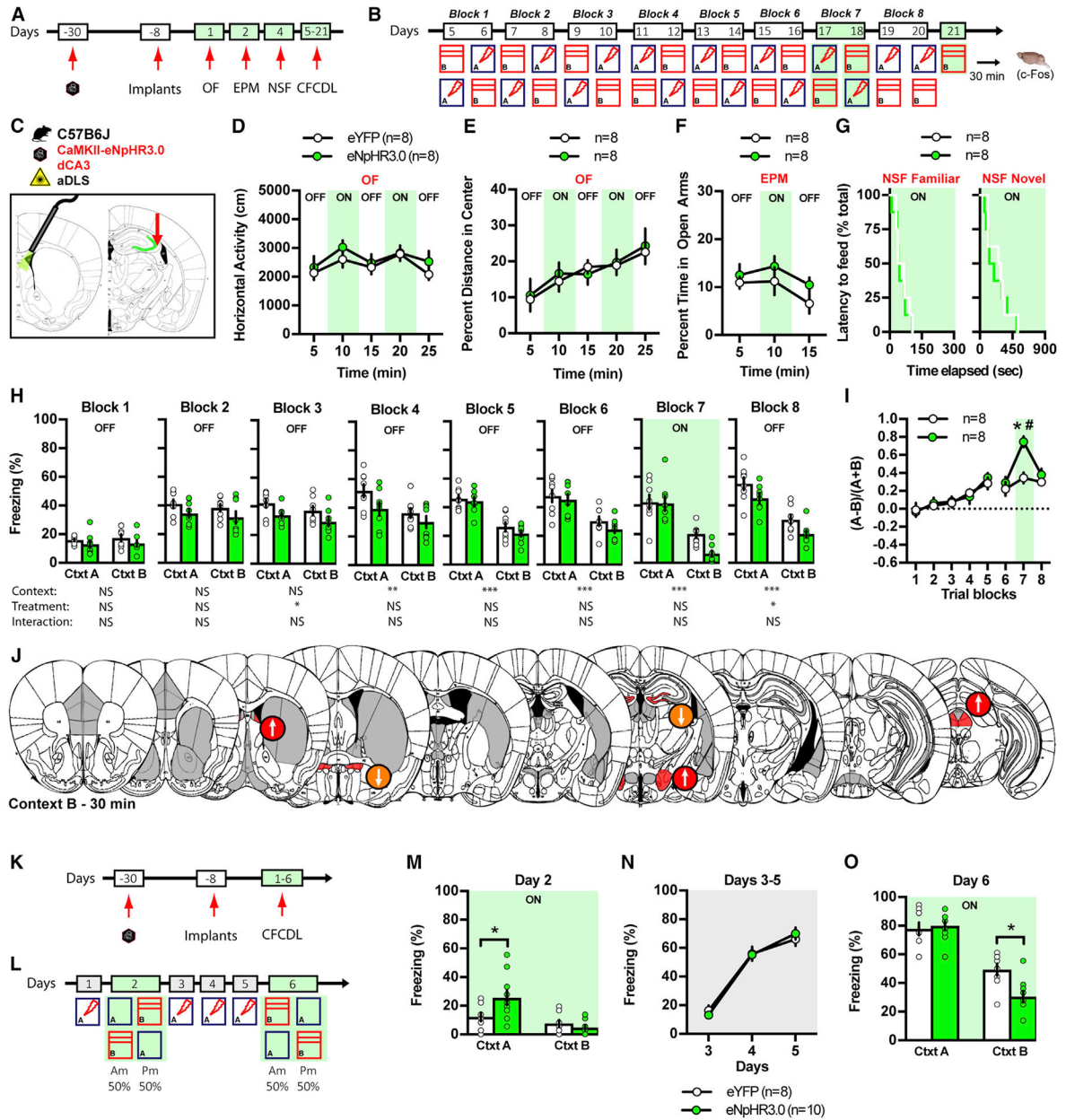


Figure 3. Dorsal CA3 Excitatory Projections to DLS Instruct Fear Responses to Ambiguous Contextual Threats

(A and B) Schematic of the behavioral timeline.

(C) Schematic illustrating dorsal CA3 infection with CaMKII-eNpHR3.0 and fiber optic implantation on top of anterior DLS in C57B6/J mice.

(D–G) Silencing dorsal CA3 terminals in anterior DLS has no effect on locomotor behavior and innate anxiety in OF (D and E), EPM (F), and NSF (G).

(H and I) Silencing dorsal CA3 terminals in anterior DLS decreases freezing behavior in context B but not A (H), which results in an increase in fear discrimination ratio on block 7 (I). Data (means ± SEM; n = 8,8 mice per group) were analyzed using mixed factor two-way ANOVA (repeated measure over time) followed by Bonferroni’s multiple comparisons post

hoc test and log-rank (Mantel Cox) test. * $p < 0.05$, eNpHR3.0 versus eYFP; # $p < 0.05$, block 7 versus block 6. Statistics detailed in Table S1.

(J) Schematic representation of the effect of light silencing dorsal CA3 terminals in DLS on brain-wide c-Fos expression 30 min following exposure to context B (day 21). Regions highlighted in red denote a significant effect of eNpHR3.0, and arrows indicate the direction of the effect.

(K and L) Schematic of the behavioral timeline.

(M–O) Silencing dorsal CA3 terminals in anterior DLS increases freezing behavior in context A but not B early on training and (M), and decreases freezing behavior in context B but not A later on training (O) following repeated training in context A (N). Data (means \pm SEM; $n = 8, 10$ mice per group) were analyzed using mixed factor two-way ANOVA (repeated measure over time) followed by Bonferroni's multiple comparisons post hoc test. * $p < 0.05$, eNpHR3.0 versus eYFP. Statistics detailed in Table S1.

See also Figures S1, S2, S3, S5, and S7.

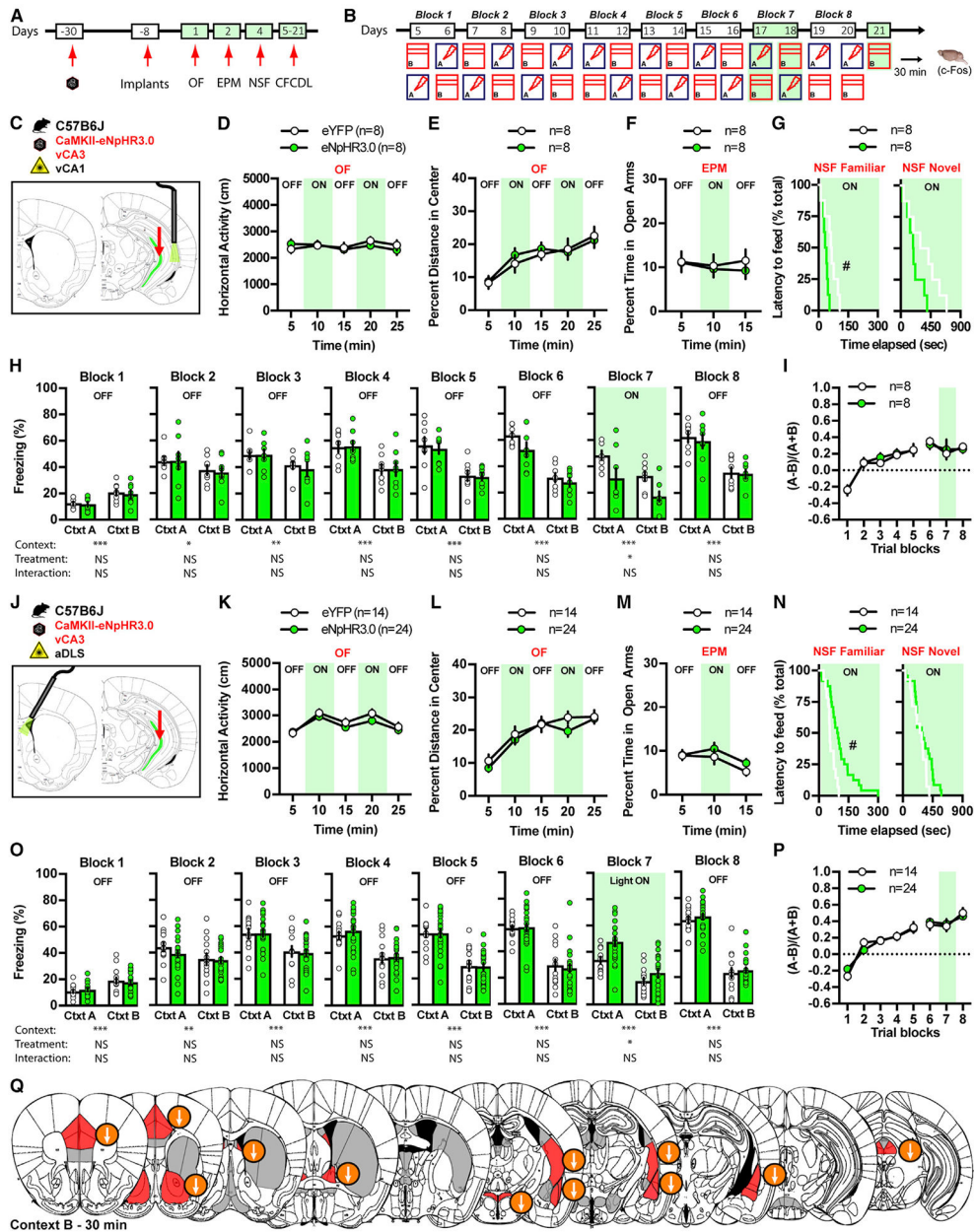


Figure 4. Ventral CA3 Excitatory Projections to CA1 and DLS Exert Opposing Roles in Gating Contextual Fear Responses

(A and B) Schematic of the behavioral timeline.

(C) Schematic illustrating ventral CA3 infection with CaMKII-eNpHR3.0 and fiber optic implantation on top of ventral CA1 in C57B6/J mice.

(D–G) Silencing ventral CA3 terminals in ventral CA1 has no effect on locomotor behavior and innate anxiety in OF (D and E) and EPM (F) while decreasing the latency to feed in the familiar environment in NSF (G).

(H and I) Silencing ventral CA3 terminals in ventral CA1 decreases freezing behavior in context A and B (H) without altering fear discrimination ratio on block 7 (I).

(J) Schematic illustrating ventral CA3 infection with CaMKII-eNpHR3.0 and fiber optic implantation on top of anterior DLS in C57B6/J mice.

(K–N) Silencing ventral CA3 terminals in DLS did not affect locomotor behavior and innate anxiety in OF (K and L) and EPM (M) while increasing the latency to feed in the familiar environment in NSF (N).

(O and P) Silencing ventral CA3 terminals in anterior DLS increases freezing behavior in context A and B (O), without altering fear discrimination ratio on block 7 (P). Data (means \pm SEM; n = 8,8 per group and n = 14,24 mice per group) were analyzed using mixed factor two-way ANOVA (repeated measure over time) followed by Bonferroni's multiple comparisons post hoc test and log-rank (Mantel Cox) test. #p < 0.05, eNpHR3.0 versus eYFP. Statistics detailed in Table S1.

(Q) Schematic representation of the effect of light silencing vCA3 terminals in aDLS on brain-wide c-Fos expression 30 min following exposure to context B (day 21). Regions highlighted in red denote a significant effect of eNpHR3.0, and arrows indicate the direction of the effect.

See also Figures S1, S6, and S7.

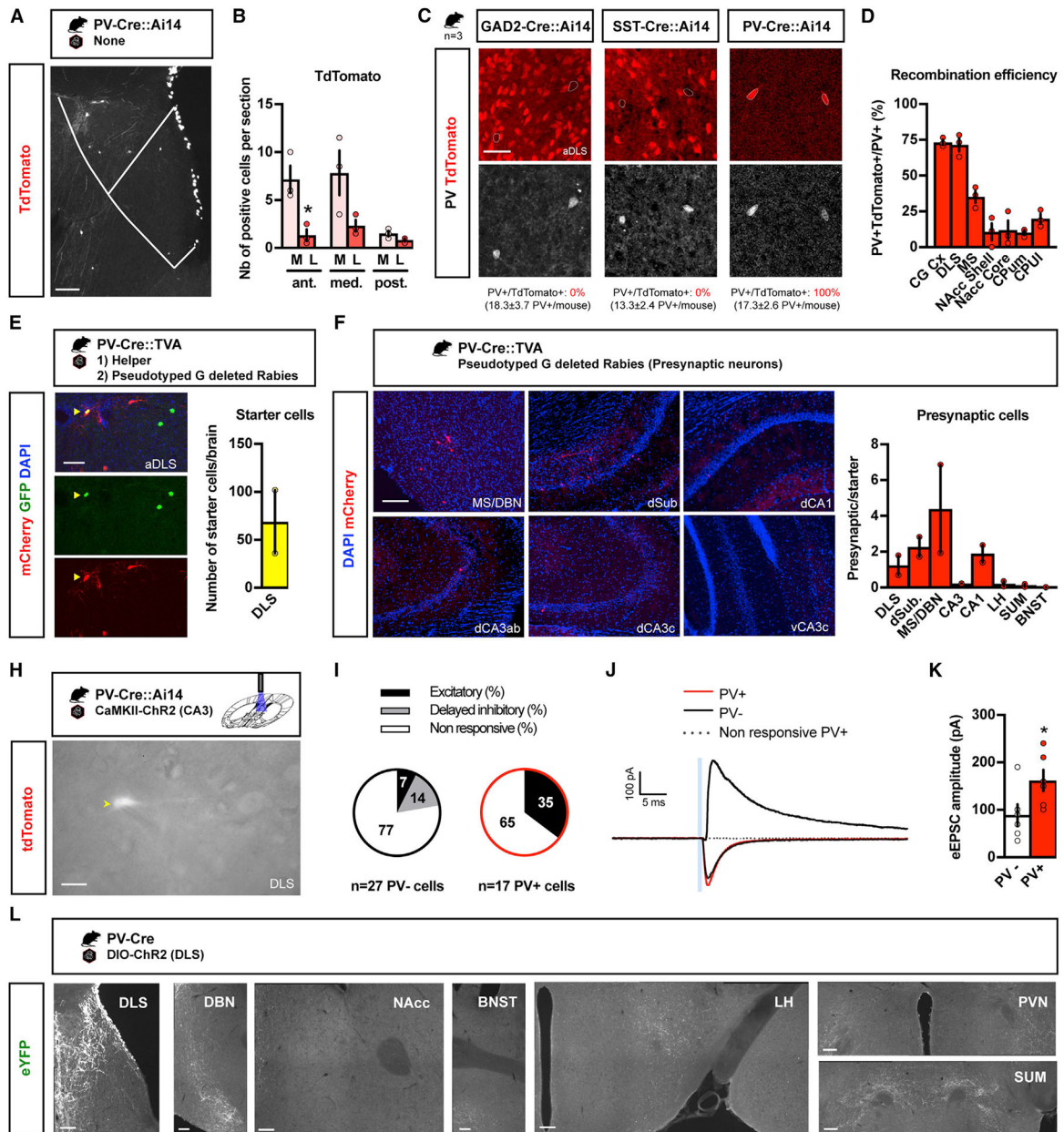


Figure 5. Characterization of DLS PV Neurons

(A) Mapping of tdTomato-expressing cells in the medial and lateral part of DLS in the progeny of PV-Cre mice bred with Ai14 mice. Scale bar: 100 μ m. Representative images for 3 independent animals. Scale bar: 100 μ m.

(B) Quantifications of tdTomato-expressing cells in DLS along the rostrocaudal and mediolateral axis. Data (means \pm SEM; n = 3 mice per group) were analyzed using paired two-tailed Student t test. *p < 0.05, medial versus lateral.

(C) Immunohistochemistry for PV and endogenous expression of tdTomato in the DLS of GAD2-Cre::Ai14, SST-Cre::Ai14 and PV-Cre::Ai14. Note the lack of overlap between PV and tdTomato in GAD2-Cre::Ai14 and SST-Cre::Ai14 mice. Representative images for 3 independent animals (single experiment). Scale bar: 25 μ m.

(D) Quantifications of the overlap of tdTomato-expressing cells with PV immunopositive cells in the cingulate cortex, DLS, MS, nucleus accumbens shell and core, and caudate putamen medial and lateral of PV-Cre::Ai14. Data (means \pm SEM; n = 3 mice per group).

(E) PV-Cre::TVA bigenic mice were injected with helper virus (AAV8-EF1a-FLEX-HB) followed by pseudotyped G-deleted rabies virus (EnvA-SAD G-mCherry) in the DLS. Yellow arrowheads denote starter cells, which are positive for both GFP (helper) and mCherry (rabies). Representative images for 2 independent animals. Scale bar: 50 μ m. Means \pm SEM; n = 2 mice per group.

(F) Presynaptic partners were identified in the MS/DBN, dorsal subiculum, dorsal CA1, and dorsal and ventral CA3. Representative images for 2 independent animals. Scale bar: 100 μ m. Means \pm SEM; n = 2 mice per group.

(H–K) CA3 provides powerful synaptic input to PV neurons in DLS.

(H) Acute slices obtained from 6-week-old PV-Cre::Ai14 bigenic mice injected with CaMKII-ChR2 into CA3 were used for *ex vivo* slice electrophysiology. Solid yellow arrowhead indicates tdTomato-labeled PV neuron. Representative image for 4 independent animals. Scale bar: 10 μ m.

(I) Light-evoked short latency (2 ± 0.7 ms) excitatory postsynaptic currents (eEPSCs) were detected in PV and non-PV neurons following CA3 terminal activation. A light-evoked delayed (46 ± 5 ms) inhibitory current (eIPSC) was observed in a subset of non-PV neurons.

(J) Example recordings of blue-light-evoked inputs onto DLS neurons. Traces show synaptic currents (EPSCs: bottom, IPSCs: top) evoked in both PV- and non-PV-expressing neurons (red and black, respectively), and the 5-ms light pulse is indicated by a blue box.

(K) Average amplitude for both cell types. Data (means \pm SEM; n = 6, 4 animals per group) were analyzed using unpaired Student two-tailed t test (detailed in Table S1).

(L) Immunohistochemistry for eYFP in the DLS, DBN, NAcc, BNST, LH, PVN, and SUM of PV-Cre mice injected with AAV5-DIO-ChR2-eYFP. Representative images for 3 independent animals (single experiment). Scale bar: 100 μ m.

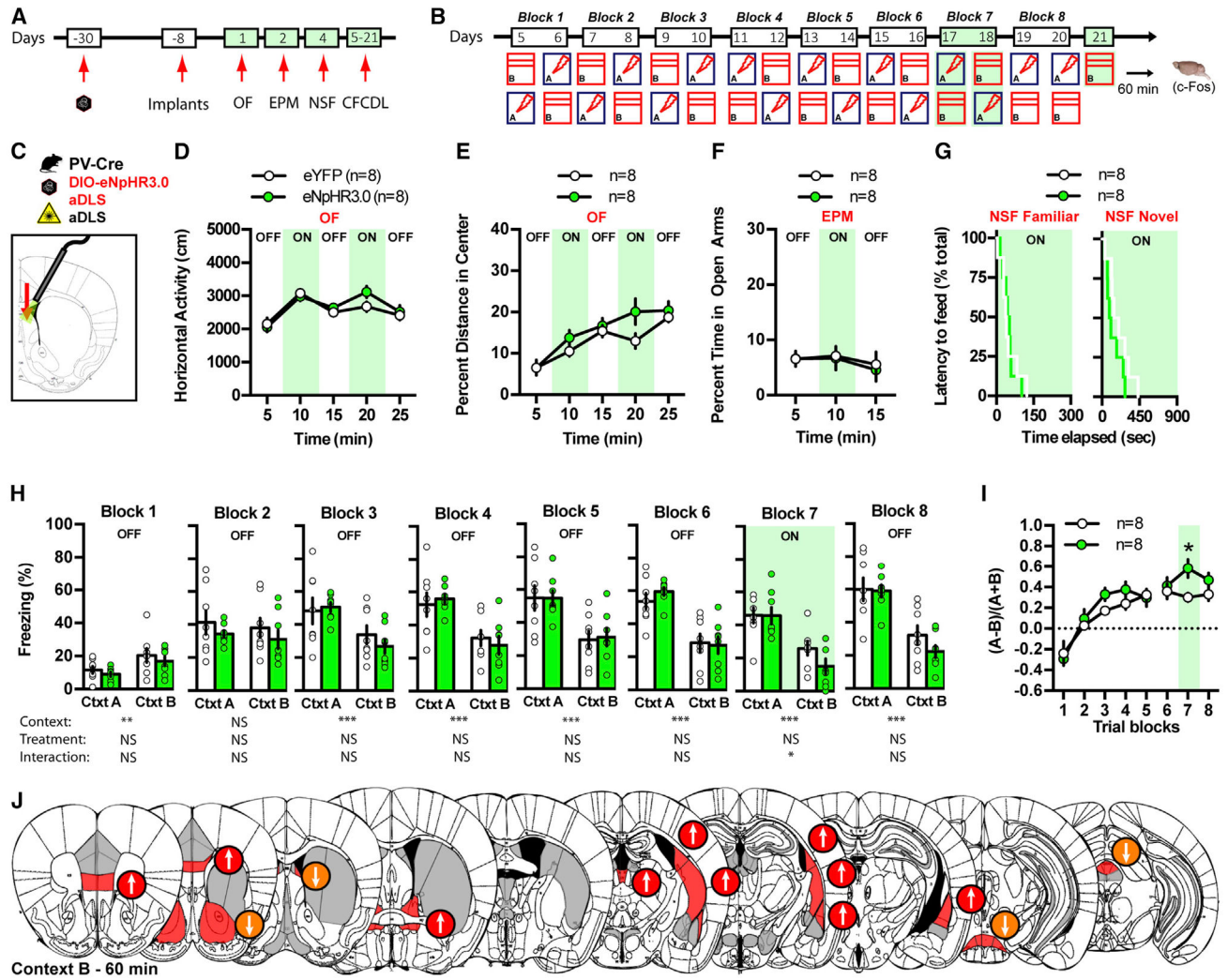


Figure 6. Optogenetic Silencing of DLS PV Neurons Increases Contextual Fear Discrimination (A and B) Schematic of the behavioral timeline. (C) Schematic illustrating infection of DLS PV neurons with DIO-eNpHR3.0 and fiber optic implantation on top of DLS in PV-Cre mice. (D–G) Silencing DLS PV neurons has no effect on locomotor behavior and innate anxiety in OF (D and E), EPM (F), and NSF (G). (H and I) Silencing DLS PV neurons decreases freezing behavior in context B but not A (H), which results in an increase in fear discrimination ratio on block 7 (I). Data (means ± SEM; n = 8,8 mice per group) were analyzed using mixed factor two-way ANOVA (repeated measure over time) followed by Bonferroni’s multiple comparisons post hoc test and log-rank (Mantel Cox) test. *p < 0.05, eNpHR3.0 versus eYFP. Statistics detailed in Table S1. (J) Schematic representation of the effect of light silencing PV neurons in DLS on brain-wide c-Fos expression 60 min following exposure to context B (day 21). Regions highlighted in red denote a significant effect of eNpHR3.0, and arrows indicate the direction of the effect. See also Figures S1 and S8.

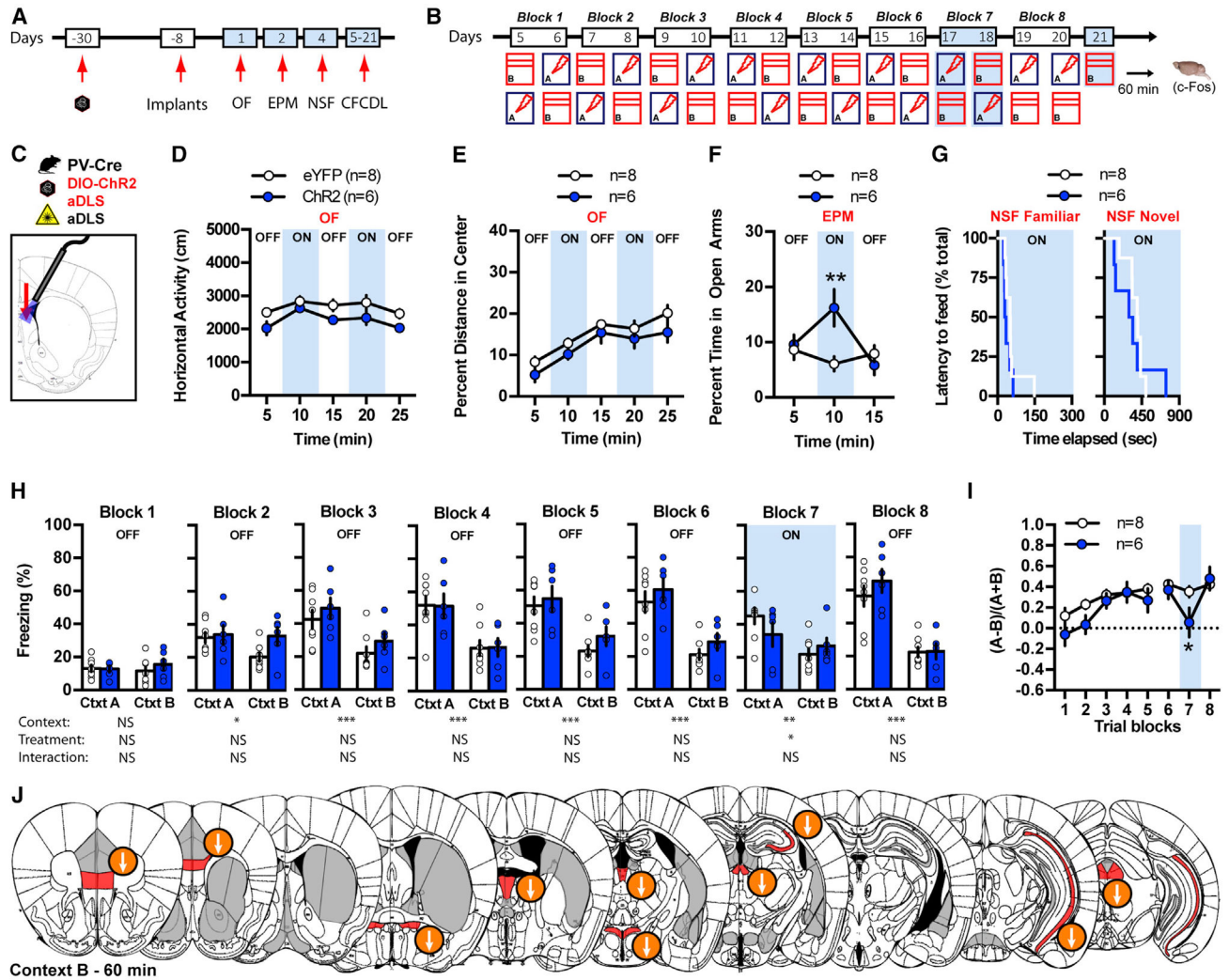


Figure 7. Optogenetic Stimulation of DLS PV Neurons Decreases Contextual Fear Discrimination

(A and B) Schematic of the behavioral timeline.

(C) Schematic illustrating infection of DLS PV neurons with DIO-ChR2 and fiber optic implantation on top of DLS in PV-Cre mice.

(D–G) Stimulating DLS PV neurons has no effect on locomotor behavior and innate anxiety in OF (D and E) and NSF (G) but induces a strong anxiolytic effect in EPM (F).

(H and I) Stimulating DLS PV neurons alters freezing behavior in both context A and B (H), which results in decrease in fear discrimination ratio on block 7 (I). Data (means ± SEM; n = 8, 6 mice per group) were analyzed using mixed factor two-way ANOVA (repeated measure over time) followed by Bonferroni’s multiple comparisons post hoc test and log-rank (Mantel Cox) test. *p < 0.05, ChR2 versus eYFP. Statistics detailed in Table S1.

(J) Schematic representation of the effect of light stimulating PV neurons in DLS on brain-wide c-Fos expression 60 min following exposure to context B (day 21). Regions highlighted in red denote a significant effect of ChR2, and arrows indicate the direction of the effect.

See also Figures S1, S2, and S8.

Author Manuscript

Author Manuscript

Author Manuscript

Author Manuscript